U.S. DEPARTMENT OF ENERGY | Office of Science

DOE/SC-ARM-TR-318

EPCAPE Radar b1 Data Processing: Corrections, Calibrations, and Processing Report

M Rocque
Y-C Feng
E Cromwell
A Matthews
V Castro
M Deng
E Schuman
I Silber
T Wendler
I Lindenmaier

June 2025

ARM

DISCLAIMER

This report was prepared as an account of work sponsored by the U.S. Government. Neither the United States nor any agency thereof, nor any of their employees, makes any warranty, express or implied, or assumes any legal liability or responsibility for the accuracy, completeness, or usefulness of any information, apparatus, product, or process disclosed, or represents that its use would not infringe privately owned rights. Reference herein to any specific commercial product, process, or service by trade name, trademark, manufacturer, or otherwise, does not necessarily constitute or imply its endorsement, recommendation, or favoring by the U.S. Government or any agency thereof. The views and opinions of authors expressed herein do not necessarily state or reflect those of the U.S. Government or any agency thereof.

EPCAPE Radar b1 Data Processing: Corrections, Calibrations, and Processing Report

M Rocque, Pacific Northwest National Laboratory (PNNL)
M Deng, Brookhaven National Laboratory
Y-C Feng, PNNL
E Schuman, PNNL
E Cromwell, PNNL
I Silber, PNNL
A Matthews, PNNL
T Wendler, PNNL
V Castro, PNNL
I Lindenmaier, PNNL

June 2025

How to cite this document:

Rocque, M, M Deng, Y-C Feng, E Schuman, E Cromwell, I Silber, A Matthews, T Wendler, V Castro, and I Lindenmaier. EPCAPE Radar b1 Data Processing: Corrections, Calibrations, and Processing Report. U.S. Department of Energy, Atmospheric Radiation Measurement user facility, Richland, Washington. DOE/SC-ARM-TR-318.

Work supported by the U.S. Department of Energy,
Office of Science, Office of Biological and Environmental Research

Acronyms and Abbreviations

AMF1	First ARM Mobile Facility
ARM	Atmospheric Radiation Measurement
ARSCL	Active Remote Sensing of Clouds Value-Added Product
DOE	U.S. Department of Energy
EIKA	Extended Interaction Klystron Amplifier
EPC	EPCAPE ARM site code
EPCAPE	Eastern Pacific Cloud Aerosol Precipitation Experiment
GE	general sensitivity mode
IOP	intensive operational period
KaSACR	Ka-band Scanning ARM Cloud Radar
KAZR	Ka-band ARM Zenith Radar
LD	laser disdrometer
LDQUANTS	Laser Disdrometer Quantities Value-Added Product
LDR	linear depolarization ratio
LT	local time
MD	moderate sensitivity mode
NEXRAD	Next-Generation Weather Radar
PPI	plan position indicator
Py-ART	Python ARM Radar Toolkit
RCA	relative calibration adjustment
RF	radio frequency
RH	relative humidity
RHI	range height indicator
RR	rain rate
SACRCOR	Scanning ARM Cloud Radar Corrections Value-Added Product
SNR	signal-to-noise ratio
TRACER	Tracking Aerosol Convection Interactions Experiment
UTC	Coordinated Universal Time
VAP	value-added product
VDIS	video disdrometer
VPT	vertically pointing scan
WRA	wet radome attenuation
WSACR	W-band Scanning ARM Cloud Radar

Contents

Figures

Tables

1.0 Introduction

The U.S. Department of Energy (DOE)'s Atmospheric Radiation Measurement (ARM) user facility recently deployed its First ARM Mobile Facility (AMF1) to La Jolla, California as part of the Eastern Pacific Cloud Aerosol Precipitation Experiment (EPCAPE) campaign. Some of the goals behind EPCAPE were to characterize the diurnal and seasonal cycles of stratocumulus clouds and to investigate the cloud-aerosol-radiation interactions and feedbacks in the area. The deployment of the AMF1 for a full year from 15 February 2023 to 14 February 2024 aided in addressing these scientific questions. While AMF1 collected data year-round, enhanced measurements were taken during two intensive operational periods (IOPs). The first IOP occurred from April to June and focused on the chemistry of low clouds (EPCAPE_Chem), while the second IOP occurred from July to September and was focused on the radiation of high clouds (EPCAPE_Radiation). Several cloud radars were deployed with AMF1 to collect valuable data on cloud properties that will help users address key science objectives.

As in past ARM campaigns, a1-level radar data is extensively analyzed and calibration techniques are performed to generate b1-level data (Matthews et al. 2023, Feng et al. 2024). Radar data at the b1-level are of the highest quality and thus can be used to examine scientific questions. The status of the a1-level data and the a1-to-b1 process for the EPCAPE radars is subsequently detailed in this document.

1.1 Overview of EPCAPE Radars

Three radars were deployed to La Jolla, California as part of the AMF1 for EPCAPE: a Ka-band ARM Zenith Radar (KAZR), a Ka-band Scanning ARM Cloud Radar (KaSACR), and a W-band Scanning ARM Cloud Radar (WSACR). KaSACR and WSACR are co-mounted and together are referred to as SACR. KAZR was located on the Scripps Pier with the main facility (M1; 32.87°N, 117.26°W) while SACR was positioned about 3 km to the SSE of M1 on Mt. Soledad at the ancillary S2 site (32.84°N, 117.25°W). Locations of the radars and surrounding terrain is shown in Figure 1 while Figure 2 depicts the installed radars at their locations. Radar specifications including frequency, gate resolution, and maximum range (among other parameters) are displayed in Table 1.

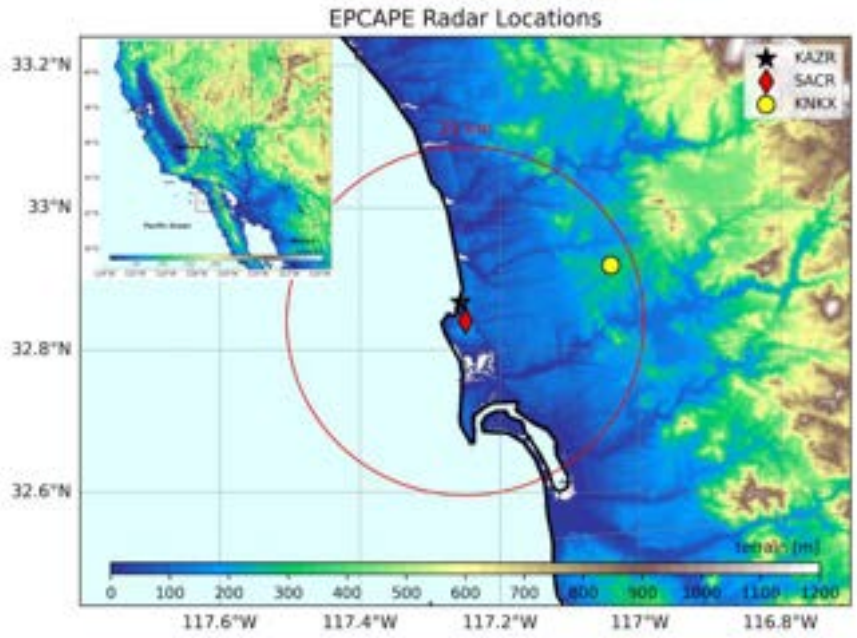

Figure 1. Location of ARM radars (KAZR: black star, SACR: red diamond) deployed during EPCAPE. KAZR is located at the main facility (M1) on the Scripps Pier while SACR is located on Mt. Soledad at the S2 site. The SACR 25-km range ring is shown in red and the San Diego WSR-88D (KNKX) is marked as the yellow dot. Terrain heights (m) are shaded and the insert depicts the southwest U.S. for context.

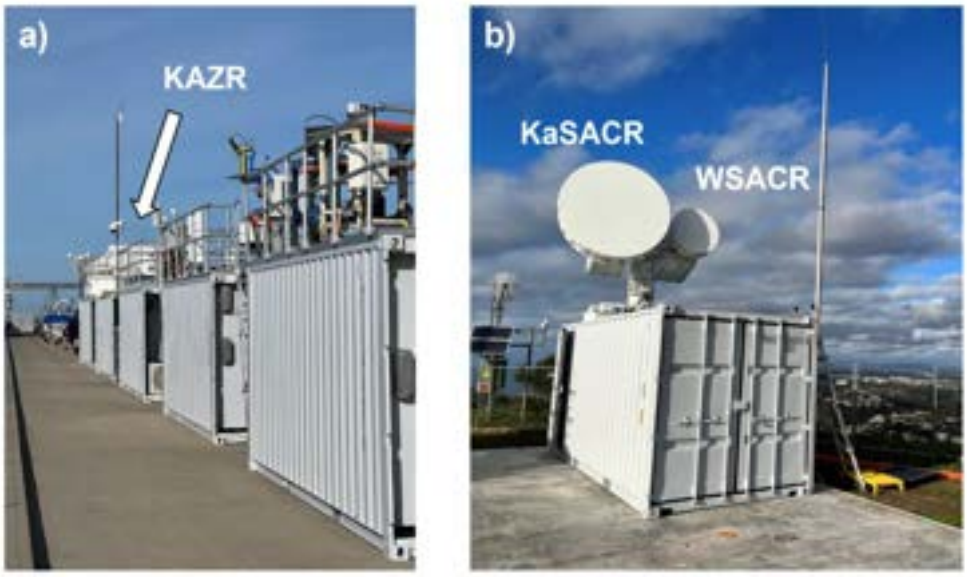

Figure 2. ARM radars installed at EPCAPE. a) KAZR depicted in the third container on the Scipps Pier (M1 site) and b) KaSACR (left; large radome) and WSACR (right; small radome) located at Mt. Soledad (S2 site).

Table 1. Specifications of each radar during EPCAPE.

Radar	Frequency (GHz)	Wavelength (cm)	Transmit power (kW)	Antenna diameter (m)	Beam width (deg)	Gate spacing (m)	Polarization	Nyquist velocity (m/s)	Maximum range (km)
KaSACR	35.3	0.85	2	1.82	0.33	24.98	single	11.80	24.2
WSACR	93.9	0.32	0.769	0.9	0.25	24.98	single	4.10	27.7
KAZR	34.9	0.86	0.162	2	0.30	29.98	single	7.97	18.1

1.2 Radar Performance

The cloud radars deployed during EPCAPE performed generally quite well throughout the campaign. Figure 3 shows the percentage of data files available for each radar compared to the maximum files available based on the scan strategy (detailed below). KAZR data is available nearly 100% of the time during the entire campaign. KaSACR and WSACR also performed well, although there were some days of no operations. Before 12 March 2023, the final scan strategy had not been set yet, which partially explains why the data availability in late February and early March is lower. Notable times of missing SACR data include: 2-6 June 2023 when the KaSACR chiller was replaced, 10-12 July 2023 when the KaSACR rotary joints were replaced, 19-22 August 2023 when Tropical Storm Hilary made landfall in southern California (SACR was stowed for safety concerns), 15-17 October 2023 when a sitewide outage occurred, 31 October-3 November 2023 when the KaSACR chiller was replaced again, and 27-29 January 2024 when a power outage occurred. If you assume SACR was 100% operational before 12 March 2023, the total performance of SACR for the entire campaign is around 92%.

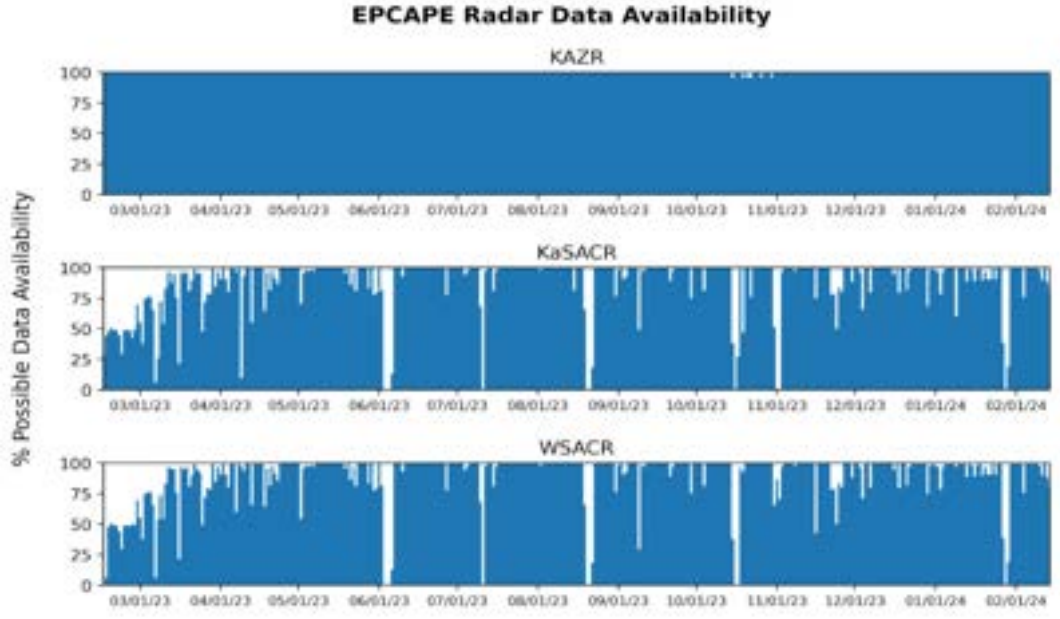

Figure 3. Radar data availability for KAZR, KaSACR, and WSACR. Percentages are calculated based on the final scan strategy set on 12 March 2023.

Time series of radar transmit power and radar sky noise are shown in Figure 4 to monitor the stability of the radar. The sky noise for each radar is consistent across the campaign. The transmit power for KAZR is also consistent with time. The transmit power for KaSACR increases substantially around 12 March 2023, which corresponds to a change in the radio frequency (RF) unit. KaSACR then stops automatically recording the output power near the end of April. Despite this, the engineering team continued to monitor the output power separately and reported minimal changes for the remainder of the campaign. Perhaps the most concerning part of Figure 4 is the steady decline in transmit power for the WSACR. This decline is attributed to a failing Extended Interaction Klystron Amplifier (EIKA), and is important to note as it will end up impacting the WSACR reflectivity offset shown later in Section 2.4.

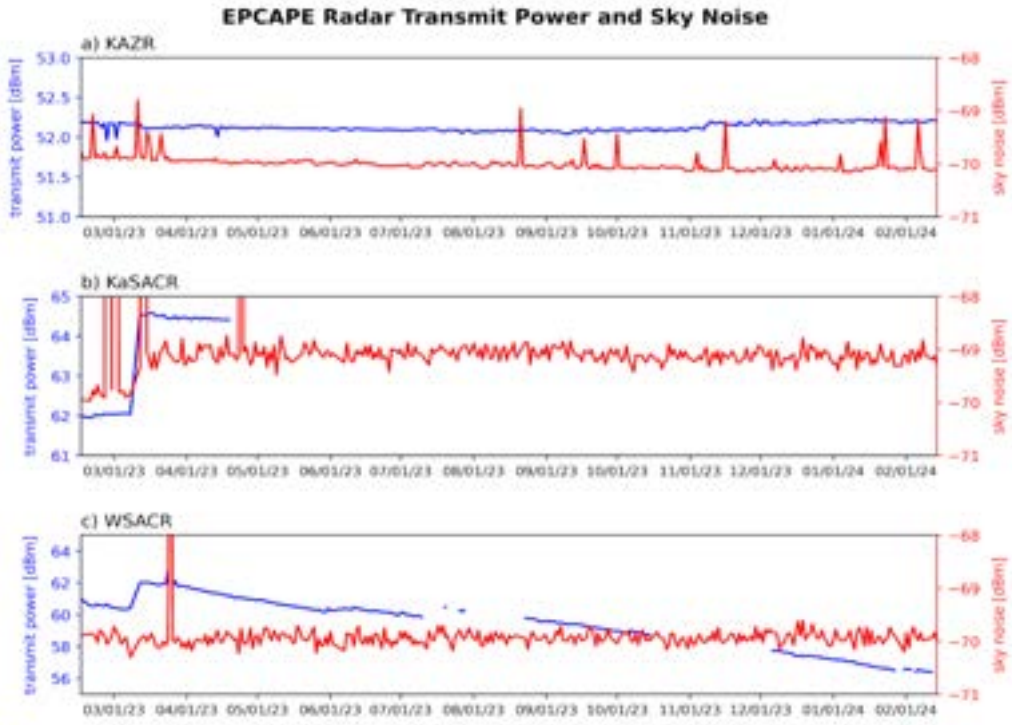

Figure 4. Time series of radar transmit power (blue) and radar sky noise (red) for the a) KAZR, b) KaSACR, and c) WSACR during EPCAPE.

1.3 Scan Strategy

Three main scans were performed by SACR during EPCAPE: a plan position indicator (PPI), a range height indicator (RHI), and a vertically pointing scan (VPT). Two different PPI scans, four different RHI scans, and one VPT scan were performed and/or repeated to create a six-hour heartbeat. A description of the different scans (including elevation and azimuth ranges) is shown in Table 2; when these scans occur during the six-hour period is shown in Figure 5. SACR is typically performing PPI1 scans, which consist of seven sweeps ranging from 0.0° to 20.0° in elevation. All PPI scans are performed over a sector to the northwest from 280-360°. There are two periods during the six-hour time frame when SACR performs scans other than PPI1. The first period begins with 13 minutes of RHI1 scans, one RHI2 scan, one VPT scan, one PPI2 scan, and 13 minutes of RHI1 scans again. RHI1 scans focus on a narrow sector centered around the KAZR location, which is 348.1° from SACR. The scan strategy is set up so that the PPI2 scan occurs at the top of the hour at 01, 07, 13, and 19 UTC (which corresponds to 18, 00, 06, and 12 LT from

March to November). These times coincide with the launch of soundings from the pier. Thus, the RHI1 scans provide high-resolution profiles of the environment within 15-20 minutes of sounding launches. The second group of RHIs (RHI3 and RHI4) occurs three hours later. RHI3 focuses on a narrow region just north of KAZR (starting at 348.1°) and RHI4 scans a narrow sector to the west (starting at 279.0°). The purpose of these scans is to provide profiles of the environment along-wind and cross-wind.

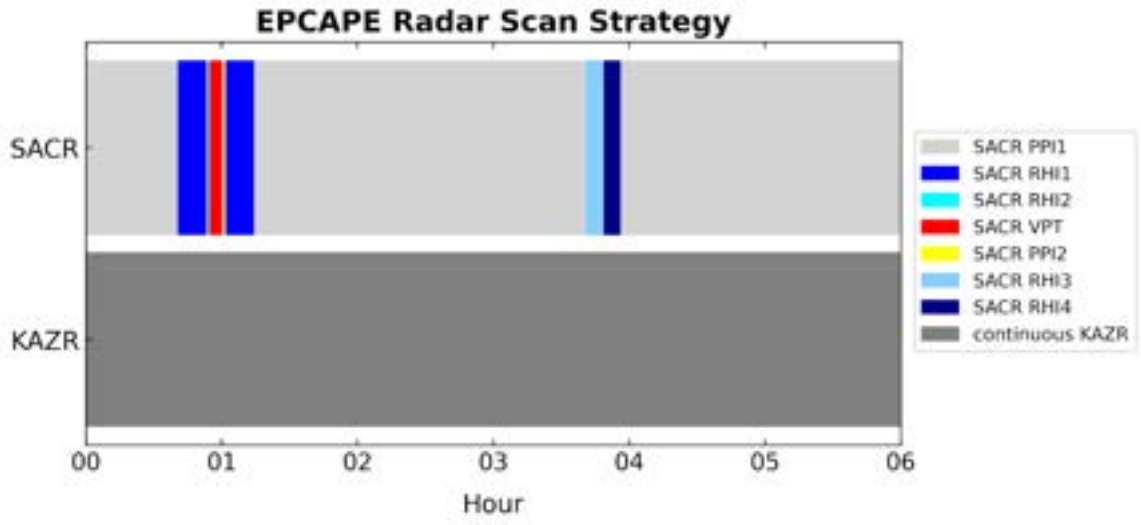

Figure 5. EPCAPE radar scan strategy with a six-hour heartbeat. SACR PPI2 scan starts at 01, 07, 13, and 19 UTC.

Table 2. Description of each radar scan type shown in Figure 5. The table includes the scan name, scan duration (minutes), elevation angles (degrees), and azimuth angles (degrees).

EPCAPE Scan Description			
Scan Name	**Scan Duration**	**Elevations (deg)**	**Azimuths (deg)**
SACR PPI1	2 min	0.0, 2.5, 5.0, 7.5, 10.0, 15.0, 20.0	280-360
SACR PPI2	< 1 min	0.0, 5.0, 10.0	280-360
SACR RHI1	13 min	-2.0-60.0	345.6-350.6 (0.5 spacing)
SACR RHI2	< 1 min	-2.0-60.0	348.1
SACR RHI3	8 min	-2.0-60.0	348.1-352.1 (0.25 spacing)
SACR RHI4	8 min	-2.0-60.0	279.0-283.0 (0.25 spacing)
SACR VPT	6 min	90	0-360

1.4 Overview of b1 Processing

As briefly mentioned earlier, the method to generate b1-level data is extensive and involves careful analysis of the a1-level data. The two main tasks in the a1-to-b1 radar data processing include calibration updates and masking. The techniques involved in these tasks will be described at a high level here.

1.4.1 Calibration

One of the key tasks in generating b1-level radar data is the calibration. Calibration involves monitoring the stability of the radar system over time and applying corrections to the radar constant, *C*. *C* can be related to the reflectivity through the logarithmic form of the radar equation:

$$Z = P_r + 20\log_{10}(r) + C$$

where *Z* is the radar reflectivity factor (dBZ), P_r is the power received (dBm), *r* is the range (km), and *C* is the radar constant (dB). A number of different terms are represented by *C* including, but not limited to, the transmitted power, the gain and beamwidth of the antenna, the dielectric constant, and the wavelength. Because of its complex nature, *C* can vary with time and thus play an important role in the accuracy of reflectivity.

Several techniques have been developed to calibrate radars, and in particular the reflectivity variable. These include engineering techniques such as corner reflector scans and solar calibrations, and data monitoring techniques such as relative calibration adjustment (RCA) and cross-comparisons with other instruments. However, the radar configuration at EPCAPE presented some challenges with calibrations that will be addressed later. Because of these challenges, the majority of the calibration analysis for EPCAPE involves comparing measurements across radars and other instruments such as disdrometers. Details on these comparisons can be found in Section 2.

1.4.2 Data Quality Masks

While most atmospheric scientists are interested in radar data from clouds and precipitation, radars measure backscatter from a number of other targets including ground clutter, terrain, biota (insects and birds), sea clutter, and even other devices that emit pulses at a similar frequency (RF interference). In an attempt to make the data more user friendly for atmospheric scientists, masks that identify hydrometeors versus non-meteorological signals are created. Each radar has at least one mask, but the methodologies for creating the masks vary depending on the radar's configuration and measured parameters. Details on the masks applied to radars deployed for EPCAPE can be found in Section 3.

2.0 Calibrations and Corrections

Radar calibration is a multi-step process that involves several techniques and considerations. Some of these techniques can be performed during the campaign, such as solar calibrations, while other techniques such as cross-comparisons with other radars are typically performed after the campaign ends. The goal of this work is to estimate the systematic bias of reflectivity for each of the radars deployed during EPCAPE. The final offsets applied to the b1 data sets are shown in Table 3, and additional details on how these offsets were determined is provided below.

Table 3. Reflectivity offsets (dB) applied to the b1 data during the indicated time frame for each radar. The last offset applied for WSACR is a linear function where t is the days since 12 March 2023.

	KAZR GE	KAZR MD		KaSACR		WSACR	
Time Frame	all	20230215 - 20230707	20230707 - 20240214	20230215 - 20230312	20230312 - 20240214	20230215 - 20230312	20230312 - 20240214
Offset (dB)	3.4	5.0	4.7	-0.2	4.2	1.0	$0.016t + 3.5$

2.1 Techniques

2.1.1 Solar Calibration

Solar calibrations can be performed to assess the radar's calibration and orientation. The solar calibration technique first involves identifying the position of the sun at a given time and location. Once the position of the sun is known, a raster scan can be completed. The sun has a known noise power that is higher than the sky noise and will thus appear as a sphere of higher power in the center of the scan. If the radar is not calibrated properly, the measured noise power of the sun will not match the expected power. If the radar is not properly aligned, the sun will not appear in the center of the scan. The solar calibrations performed by the engineering team during and after EPCAPE are primarily used to assess the antenna's pointing accuracy. Some results of the solar calibrations performed on the horizontal channel are shown in Figure 6. Even though there were some clouds present during these scans, the azimuth and elevation errors are within one beamwidth (0.3°), indicating the orientation of the radars is accurate.

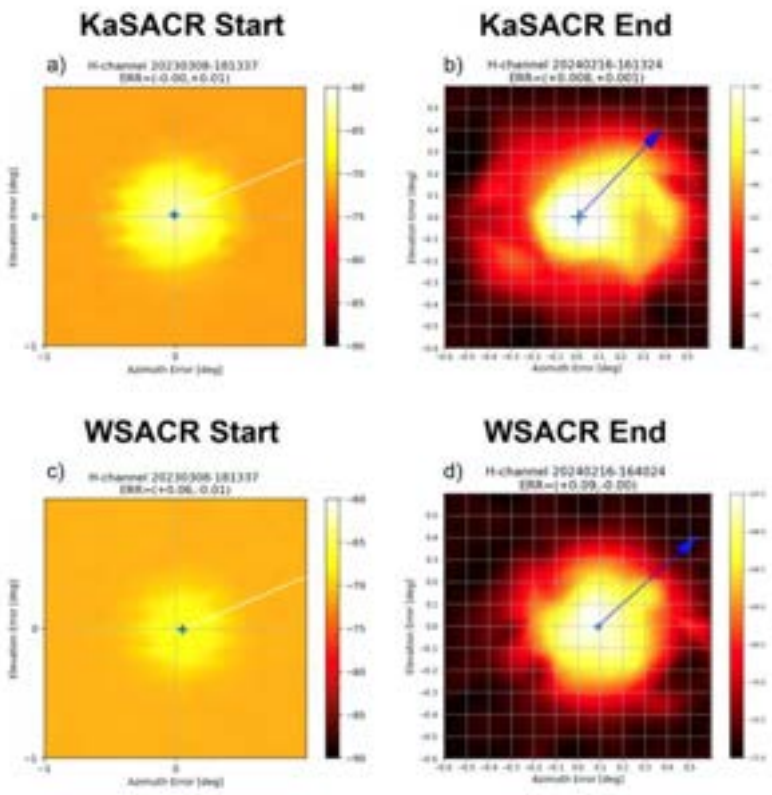

Figure 6. Results from the solar calibrations performed on 8 March 2023 (left) and 16 February 2024 (right) for the horizontal channels of KaSACR (top) and WSACR (bottom). Note the different grid sizes and power ranges (dBm) between each panel to accommodate for clouds.

2.1.2 Relative Calibration Adjustment

During EPCAPE, KaSACR often observed clutter to the north associated with the coastline and the terrain (Figure 1). While the lowest elevation angle was typically 0.0° during EPCAPE, a few scans at -0.5° elevation were performed before and after the campaign. Four PPIs of reflectivity and mean Doppler velocity are shown in Figure 7 that highlight the clutter and second-trip echoes over the ocean associated with terrain up to 100 km away. A beam blockage plot is also shown in Figure 7e that indicates the -0.5° elevation is blocked to the north, but the 0.0° elevation is not. This suggests that clutter observed at 0.0° is due to anomalous beam propagation.

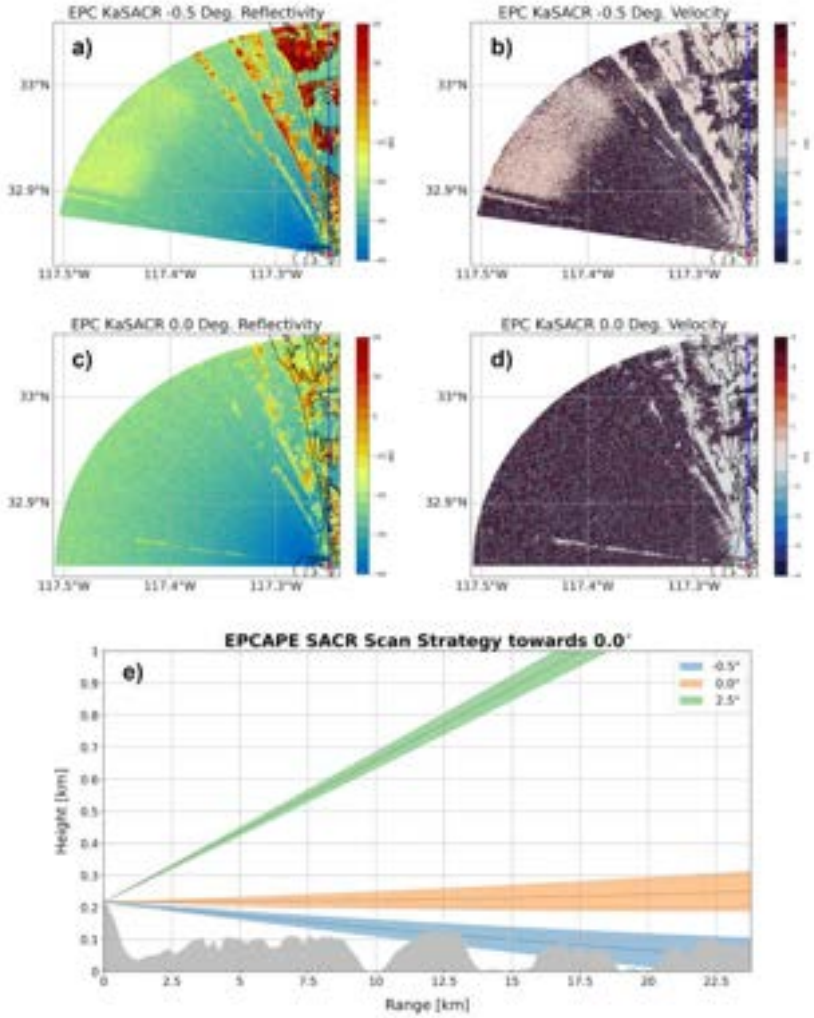

Figure 7. Sector PPIs from KaSACR on a clear day showing the reflectivity and mean Doppler velocity of ground clutter at a-b) -0.5° and c-d) 0.0° elevation. The thin blue line in each plot indicates 0.0° in azimuth. e) Beam paths towards 0.0° (North) at -0.5° (blue), 0.0° (orange), and 2.5° (green) elevation with terrain shaded in grey.

One technique that is often used to assess the stability of scanning radars is RCA. This technique involves monitoring the reflectivity of ground clutter near the radar over time (Silberstein et al. 2008, Wolff et al. 2015, Hunzinger et al. 2020). Daily mean reflectivity values of ground clutter tend to be within 0.5-1.0 dB, and fluctuations beyond 1.0 dB can indicate an issue with the radar hardware. Here we evaluate the effectiveness of using an RCA method that was developed for the Tracking Aerosol Convection Interactions Experiment (TRACER) campaign (Feng et al. 2024) during EPCAPE. Figure 8 shows the mean, 95th percentile, and 75th percentile ground clutter reflectivity for -0.5° elevation PPI scans between 350° and 0° azimuth, between 1.5 and 10 km range, with reflectivity greater than 15 dBZ, and with absolute mean Doppler velocity less than 0.2 m s^{-1} on 14 February 2023 (before the campaign start) and 16 February 2024 (after the campaign end). There is very little fluctuation in the mean, 95th, and 75th percentiles throughout both days, and the values are also similar before and after the campaign.

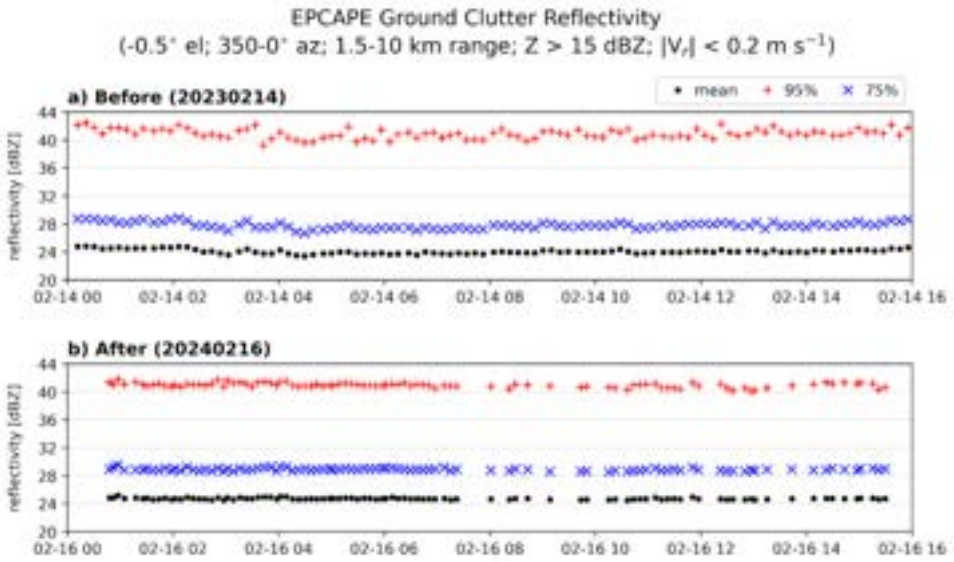

Figure 8. KaSACR RCA analysis from a) before EPC on 14 February 2023 and b) after EPC on 16 February 2024. Ground targets are selected at -0.5° elevation between 350-0° azimuth and 1.5-10 km away from the radar and have at least 15 dBZ reflectivity and an absolute mean Doppler velocity less than 0.2 m s^{-1}. Mean reflectivity is shown as the black dots, the 95th percentile is shown as the red plus signs, and the 75th percentile is shown as the blue crosses.

2.1.3 Radar Cross-Comparisons

Reflectivity values can be compared across radars to determine how well calibrated the systems are. This often requires matching radar volumes between radars and applying certain thresholds to ensure other uncertainties due to attenuation or differing scattering regimes are accounted for as best as possible. Typically, parameters such as signal-to-noise ratio (SNR) and linear depolarization ratio (LDR) are used to ensure the volumes being compared contain hydrometeors and not non-meteorological echoes. Other thresholds including relative humidity, reflectivity, and the height at which comparisons are done can be used to minimize the impacts of attenuation on the results. Table 4 shows the radar comparisons and the list of thresholds/restrictions applied to the data. Further details on these comparisons will be described later.

Table 4. Thresholds applied for each comparison study including reflectivity (dBZ), SNR (dB), LDR (dB), correlation coefficient (RhoHV), height (km), relative humidity (RH; %), rain rate from the disdrometer (RR; mm hr^{-1}), number of good points (pts), and standard deviation (σ; dB).

Radars	Reflectivity (dBZ)	SNR (dB)	LDR (dB)	RhoHV	Height (km)	Other
KAZR vs KNKX	-5 to 15	> 0	< -15	> 0.95	< 1 km	RH < 90% σ < 5.5
KaSACR vs KNKX	-5 to 15	> 0	N/A	> 0.95	none	none
KAZR vs KaSACR	-5 to 15	> 0	< -15	N/A	< 1.5 km	RH < 90% pts > 10 σ < 5

Radars	Reflectivity (dBZ)	SNR (dB)	LDR (dB)	RhoHV	Height (km)	Other
KAZR vs WSACR	-15 to 5	> 0	< -15	N/A	< 1.5 km	RH < 90% RR < 0.1 mm hr^{-1} pts > 25 σ < 4
KAZR GE vs MD	-5 to 15	> 0	none	N/A	none	pts > 1000 σ < 1.5

2.1.4 Disdrometer Cross-Comparisons

Other instruments such as ground-based disdrometers can also be compared with radars to assess the quality of reflectivity. One key uncertainty in estimating the systematic bias in reflectivity from radar is the impact of a wet radome. During rain events, water can accumulate on the radome and form a film. Significant attenuation can result depending on the thickness of the film, which in turn depends on the rain rate. Collocated disdrometers can be used to estimate the wet radome impact through a method called the wet radome attenuation (WRA) calibration technique (Deng et al. 2024). The difference in reflectivity between the disdrometer and the radar can be related to the rain rate in light and moderate rain:

$$Z_{dis} - Z_{rad} = a + b \log_{10}(RR)$$

where Z_{dis} is the disdrometer reflectivity (dBZ), Z_{rad} is the radar reflectivity (dBZ), RR is the rain rate measured from the disdrometer (mm hr^{-1}), and a and b are the resulting coefficients of the fitted logarithmic equation. If the disdrometer is assumed to be "truth", this relationship can be used to estimate the systematic bias in the radar reflectivity. For small rain rates, the WRA is assumed to be negligible, and thus the resulting bias in disdrometer and radar reflectivity can be attributed to systematic bias. Further discussion on the relationship derived from EPCAPE data can be found in Section 2.2.

2.1.5 Gas Attenuation

Attenuation due to atmospheric water vapor, while often negligible for longer-wavelength precipitation radars, is important to consider for cloud radars. The theoretical gas attenuation at Ka- and W-band for dry and moist profiles observed during EPCAPE is shown in Figure 9. For the dry profile, Ka-band gas attenuation in the vertical is less than 0.1 dB and less than 0.7 dB for W-band. However, for the moist profile that was taken during Tropical Storm Hilary, there is considerable deviation in gas attenuation between Ka- and W-bands, with W-band attenuation greater than 10 dB at 10 km. This water vapor attenuation can be even stronger in the horizontal, making it crucial to consider when performing cross-comparisons with other radars. While gas attenuation is not ultimately included in the b1-level data, it is calculated in the c1-level data for KAZR in the Active Remote Sensing of CLouds (ARSCL) value-added product (VAP) and for SACR in the Scanning ARM Cloud Radar Corrections (SACRCOR) VAP.

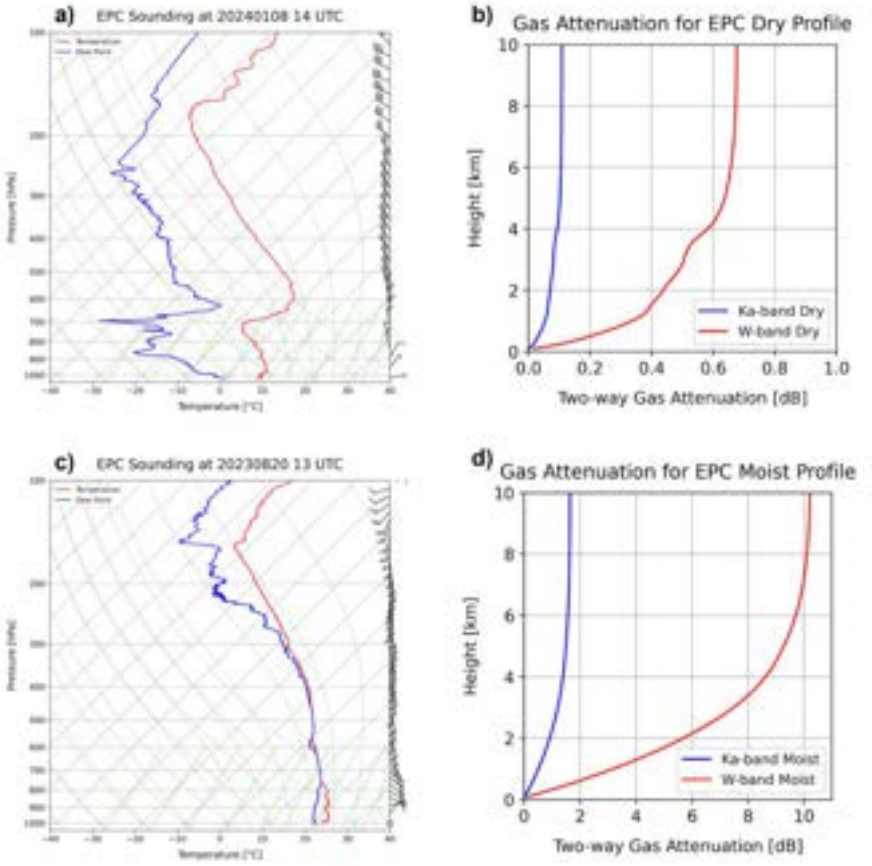

Figure 9. a) Skew-T log-p diagram from the 8 January 2024 14 UTC EPC sounding depicting a dry environment. Red (blue) line is the temperature (dew point) (°C) and the wind barbs are plotted on the right axes (m s^{-1}). b) Profile of the two-way gas attenuation (dB) for Ka-band (blue) and W-band (red) for the dry environment shown in a). c) As in a) but the sounding is from 20 August 2023 at 13 UTC and represents a moist environment. d) As in b) but for the corresponding moist environment shown in c).

2.2 KAZR Corrections

KAZR operated in two modes during EPCAPE, general (GE) and moderate (MD) sensitivity. One of the key differences between the two modes is the pulse that is emitted from the radar. In the MD mode, the pulse is chirped (frequency-modulated) and longer compared to the GE mode. This pulse compression results in the MD mode having higher sensitivity but a larger blind zone close to the surface. For EPCAPE, the MD blind zone was quite large, resulting in lack of valid data below about 1 km.

In addition to the two operating modes, this KAZR was upgraded to receive both co- and cross-polarized signals (while emitting a single polarization), and is thus referred to affectionately as KAZR1.5. This means that in addition to standard variables such as reflectivity, Doppler velocity, spectral width, and SNR, LDR is also collected. The use of LDR is particularly important in the detection of non-meteorological signals, which will be discussed further in Section 3. For the purpose of calibration, the sole focus is on correcting the reflectivity. KAZR systematic biases in reflectivity are computed

through several different techniques. Two methodologies involve comparisons of the KAZR GE mode with other instruments including the nearby WSR-88D (KNKX, San Diego) and a surface laser disdrometer. The GE and MD modes can then be compared, and the MD mode can be corrected based on the GE mode. Results from these methodologies are described further.

2.2.1 Methodology Overviews and Uncertainty

2.2.1.1 KAZR versus KNKX Cross-Comparison

The WSR-88D closest to EPCAPE is KNKX, San Diego, which is located about 20 km ENE of the main facility (32.92°N, 117.04°W). KNKX is an S-band radar operated by the National Weather Service. Because of the high quality and frequent calibrations of the Next-Generation Weather Radar (NEXRAD) system, we use the WSR-88Ds as "ground truth". Vertical profiles over KAZR are extracted from the KNKX PPIs using the `columnsect` utility in the Python ARM Radar Toolkit (Py-ART; Helmus and Collis 2016) module. These points are then compared with the nearest in time and range KAZR points. In total, data from 31 cases were analyzed, ranging from shallow boundary-layer clouds to stronger precipitating convection.

2.2.1.2 KAZR versus LD Cross-Comparison

One laser disdrometer (LD) and one video disdrometer (VDIS) were deployed at the main site for EPCAPE. Both disdrometers have associated VAPs that have parameters such as reflectivity at different frequencies (S-band, C-band, Ka-band), specific attenuation, drop size distributions, and rain rates. Here, reflectivity estimated from the LD is compared with KAZR GE mode reflectivity at 500 m via the WRA technique detailed in Deng et al. (2024). The differences between the disdrometer and KAZR reflectivity are compared with rain rates, and a best fit line following the equation in Section 2.1.4 is computed. The resulting equation estimates the impact of WRA. To find the systematic bias, the rain rate in the equation can be set to 0.05 mm hr^{-1} where WRA is assumed to be negligible.

2.2.1.3 Uncertainty Estimates Visualized through a Case Study

Before the general results from the two methodologies are presented, a case study analysis is provided to highlight the importance of different thresholds when comparing reflectivity across instruments and the impact of other uncertainties in KAZR reflectivity that are not related to systematic biases. Figure 10 shows profiles of reflectivity from KNKX and KAZR on 5 February 2024. Stronger reflectivity values throughout the column are visible after around 16 UTC from KNKX, but reflectivity from KAZR is about 10-20 dB lower. Reflectivity at the lowest level (~ 500 m) from KNKX and KAZR is then compared with reflectivity from the LD Quantities VAP (LDQUANTS) in Figure 11. KAZR and KNKX reflectivity tend to agree fairly well before 16 UTC when the reflectivity is less than 15 dBZ, the relative humidity is less than 90%, and the rain rates are weak. After 16 UTC, a large deviation between KAZR reflectivity and KNKX and disdrometer reflectivity is observed. This deviation is related to a rapid increase in rain rate, larger reflectivity values, and an increase in relative humidity. Hydrometeor attenuation can be estimated from the disdrometer and relationships between attenuation and reflectivity and rain rate can be calculated (Figure 12). Rain rates greater than 4 mm hr^{-1} can result in at least 2 dB km^{-1} of specific attenuation. While hydrometeor attenuation can explain some of the deviation in KAZR reflectivity, the impact of

condensation and water build-up on the radome leading to WRA likely explains most of the reduction in KAZR reflectivity. It is important to note that this bias in reflectivity is not related to the systematic bias, and thus is not corrected for in the b1 data. Users should be cautious of using KAZR data in heavy rain unless they plan to thoroughly account for these additional uncertainties/impacts on reflectivity.

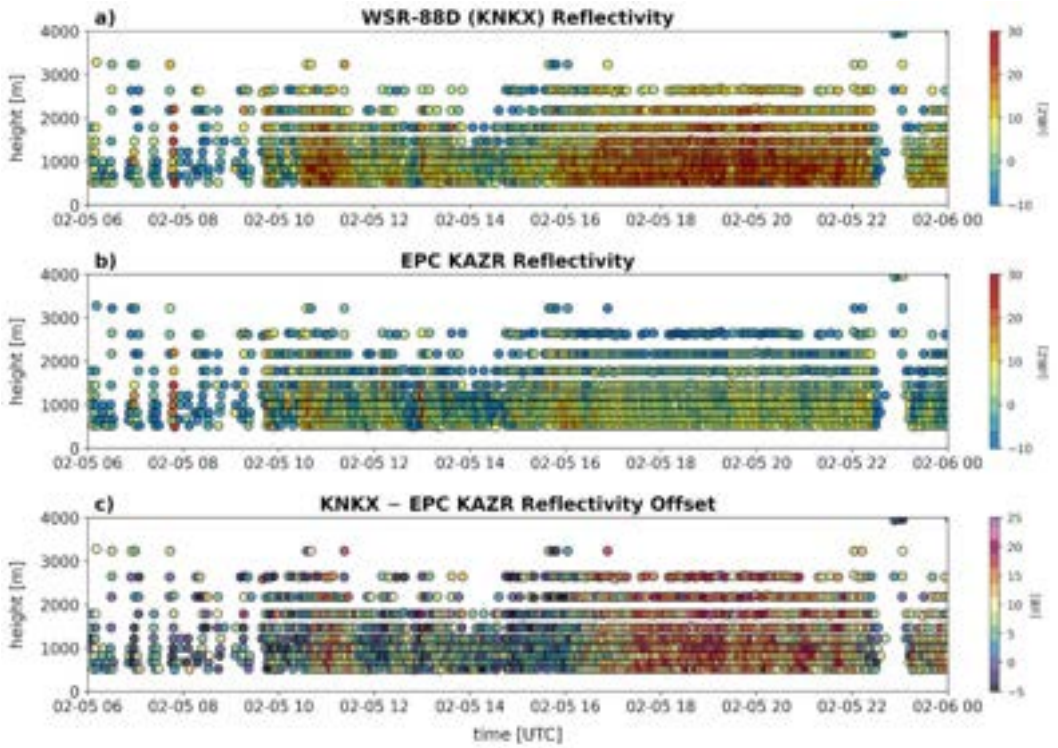

Figure 10. Profiles of a) KNKX reflectivity, b) KAZR reflectivity, and c) difference between KNKX and KAZR reflectivity from 0-4 km for 5 February 2024 from 06-00 UTC. Each dot is colored by reflectivity (or difference in reflectivity) and represents the comparison time and height between KNKX and KAZR.

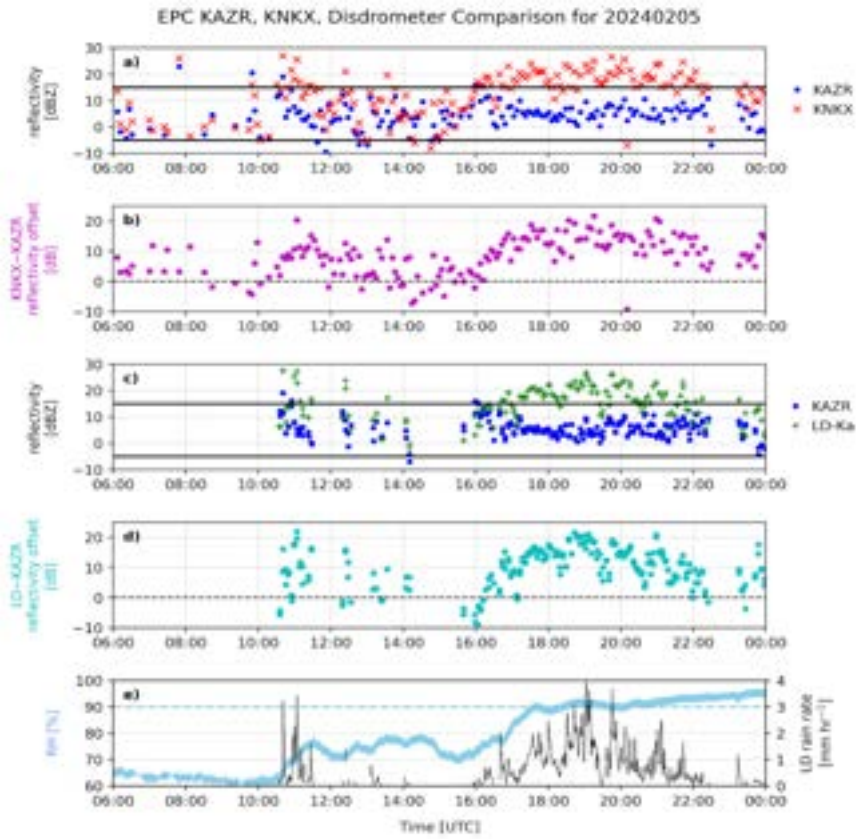

Figure 11. Time series of variables from the 5 February 2024 case from 06-00 UTC. a) KAZR GE reflectivity (blue dot) and KNKX reflectivity (red cross) with -5 and 15 dBZ thresholds highlighted, b) reflectivity difference between KNKX and KAZR (magenta star), c) KAZR GE reflectivity (blue dot) and LDQUANTS Ka-band reflectivity (green plus) with -5 and 15 dBZ thresholds highlighted, d) reflectivity difference between LD and KAZR GE (teal star), and e) relative humidity from the surface meteorological station (light blue line) and rain rate from the LD (mm hr-1; black line).

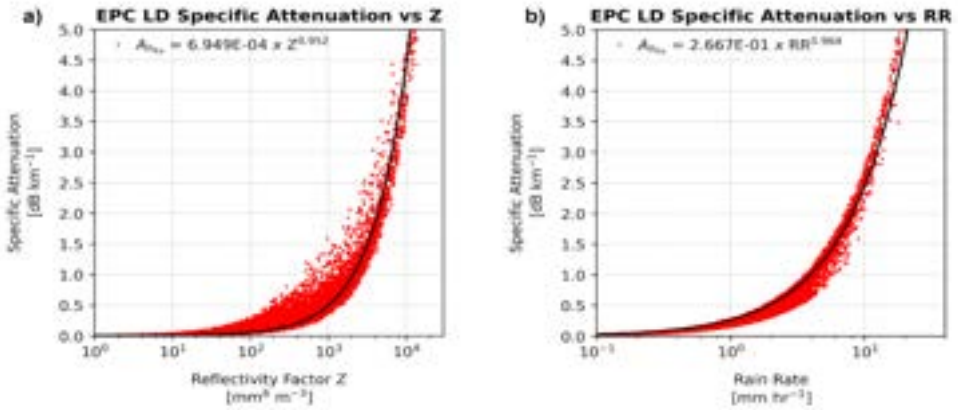

Figure 12. a) Specific attenuation (dB km^{-1}) compared with reflectivity factor (mm^6 m^{-3}), and b) specific attenuation (dB km^{-1}) compared with rain rate (mm hr^{-1}) measured by the LD at Ka-band frequency. Equations relating attenuation (A_{hKa}) to reflectivity factor or rain rate are shown in the upper left of each panel.

2.2.2 Cross-Comparison Results

As detailed above, several factors need to be considered when comparing reflectivity across radars and across instruments. For the KAZR versus KNKX analysis, several sensitivity tests were performed to determine which parameters and thresholds were best to use to ensure the systematic bias in reflectivity was calculated and not biases related to other uncertainties such as gas, hydrometeor, and WRA or different scattering regimes between Ka- and S-band. Select results from some of these sensitivity tests are shown in Figure 13. KAZR thresholds used include SNR greater than 0 dB and LDR less than -15 dB, while KNKX points had to have a correlation coefficient (RhoHV) value greater than 0.95. Additionally, KAZR was corrected for gas attenuation (following Ulaby et al. 1981), comparison points were limited to below 1 km to reduce the impacts of hydrometeor attenuation, and only times when the surface meteorological station relative humidity was less than 90% were considered to reduce the potential impacts of condensation on the radome. Offsets were also calculated for points with reflectivity between -5 and 15 dBZ to reduce the impacts of attenuation and Rayleigh versus Mie scattering. The resulting offset between KNKX and KAZR with all these thresholds applied is about 3.8 dB.

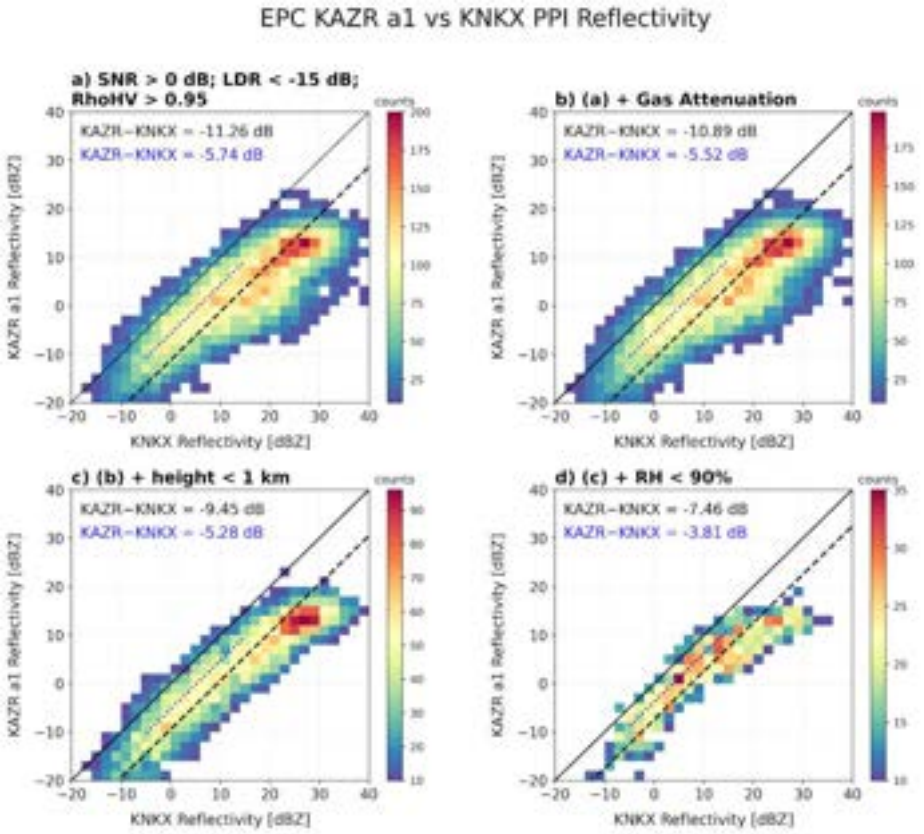

Figure 13. Histograms of KAZR a1 reflectivity (dBZ) versus KNKX reflectivity (dBZ), with colors corresponding to the number of points within each bin. a) Points with SNR greater than 0 dB, LDR less than -15 dB, and RhoHV greater than 0.95, b) points in a) and gas attenuation applied, c) points in b) and below 1 km, and d) points in c) and relative humidity less than 90%. Each panel has a one-to-one line (solid black), a fitted line for all data points (dashed black), and a fitted line for reflectivity between -5 and 15 dBZ (blue dotted). The offsets for the fitted lines are shown in the upper left of each plot.

In addition to histograms of the reflectivities of KNKX and KAZR, a time series of the daily average differences between KNKX and KAZR is plotted in Figure 14 to show the case-to-case variability. While some cases are above or below the mean, there is no noticeable trend in either direction, suggesting KAZR is stable across the campaign. The average of the daily mean differences is about 3.4 dB.

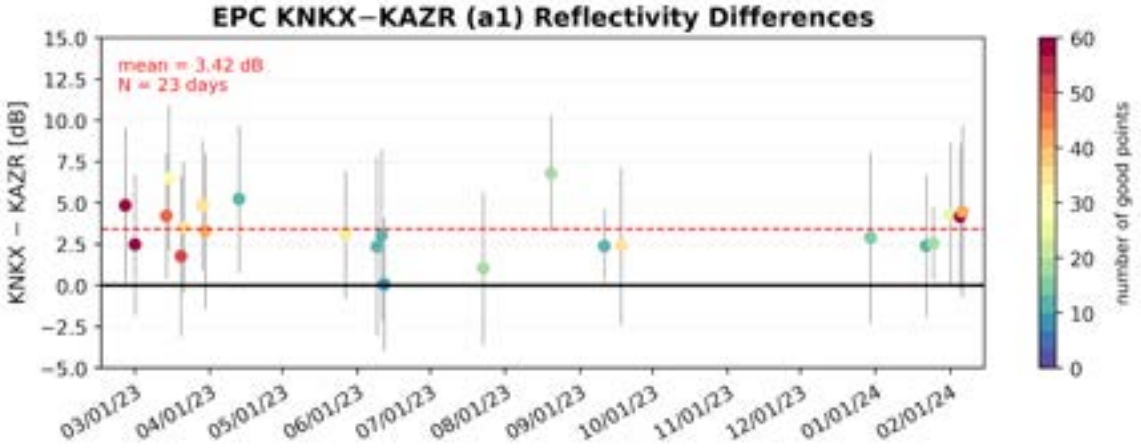

Figure 14. Time series of the daily mean differences between KNKX and KAZR reflectivity (dB). Each point is colored by the number of good points, and the error bars represent the standard deviation for that day. The mean of the daily mean differences is shown in the upper left (3.42 dB), and is plotted as the red dashed line. 23 days of data were used.

Differences between the disdrometer and KAZR GE mode reflectivity using the WRA calibration technique were calculated for each day during EPCAPE and results are displayed as a time series in Figure 15. The differences are consistent across the campaign, and the average difference is about 3.1 dB, which agrees well with the KAZR-versus-KNKX analysis.

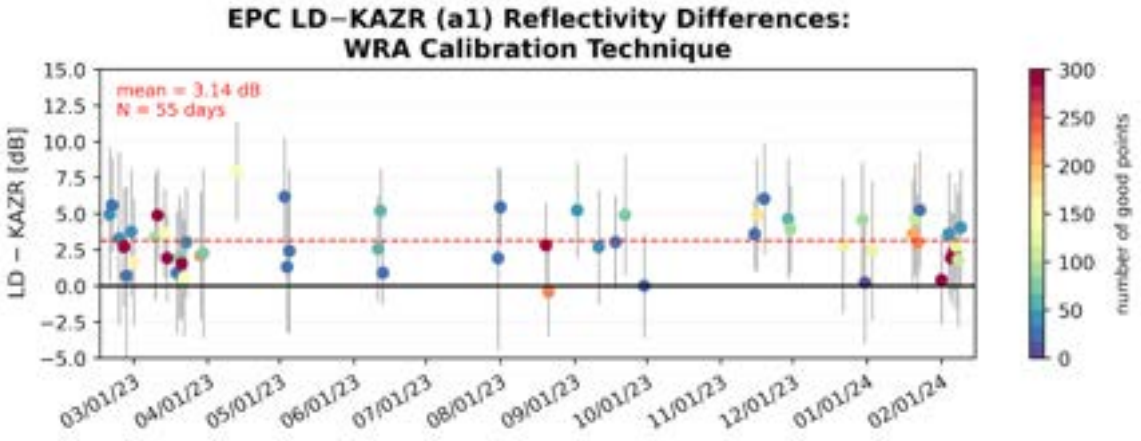

Figure 15. As in Figure 14 but with LD data using the WRA calibration technique. The resulting mean of daily mean differences between the LD and KAZR GE a1 data is 3.1 dB.

After extensive comparisons between KAZR and KNKX and the LD, an offset of 3.4 dB was applied to the KAZR GE mode reflectivity. The new KAZR data was then compared with KNKX again and the offsets were less than 1 dB (Figure 16), which is within the estimated uncertainty for this analysis.

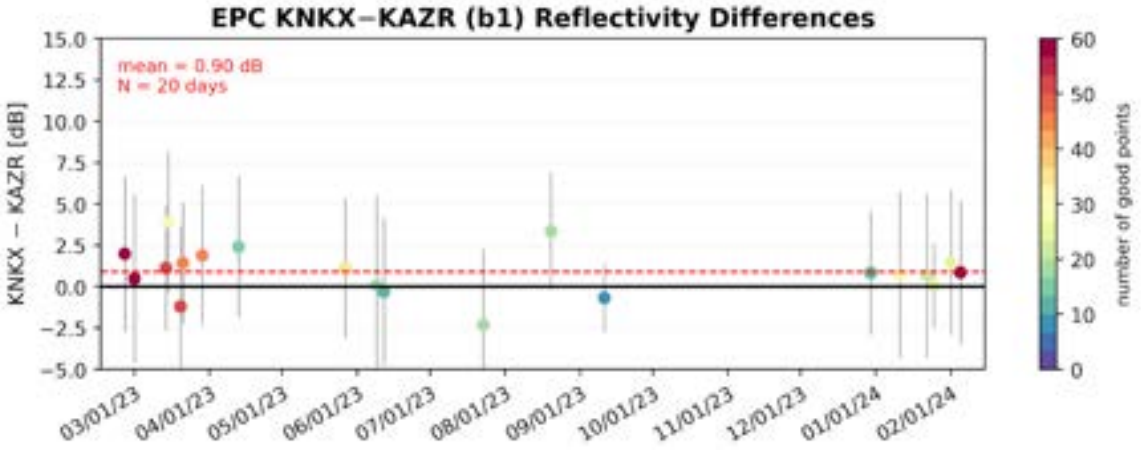

Figure 16. As in Figure 14 but with KAZR b1 data which has a 3.4 dB offset applied. The new resulting mean of daily mean differences is 0.9 dB.

To estimate some of the uncertainty between different instruments, KNKX reflectivity at 500 m is compared with LDQUANTS S-band reflectivity (Figure 17). The results suggest that the disdrometer reflectivity is about 1.9 dB higher than KNKX reflectivity on average. Thus, from using different techniques, we can estimate the uncertainty of the systematic bias to be around 2 dB, which is typical for radar studies.

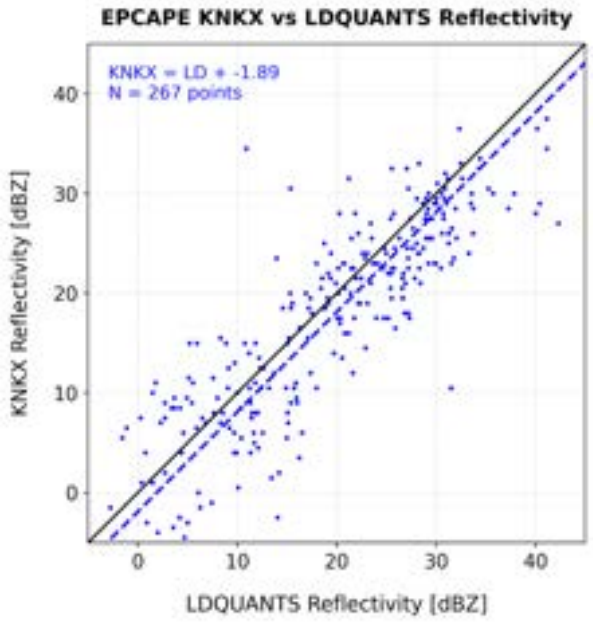

Figure 17. KNKX reflectivity (dBZ) versus LDQUANTS S-band reflectivity (dBZ). KNKX reflectivity is 1.9 dB lower than LD reflectivity on average (dashed blue line, based on 267 samples).

2.2.3 KAZR Intermode Comparison

Prior to any corrections, the KAZE GE and MD mode reflectivities were compared. First, the GE and MD data were interpolated to the same time and range. Then points were compared when the SNR was greater

than 0 dB and the reflectivity was between -5 and 15 dBZ, and daily means were computed. A time series of the daily mean differences between GE and MD mode is shown in Figure 18 when the number of good points was greater than 1000 and the standard deviation of the points was less than 1.5 dB. The difference is stable in time, but a small shift can be observed in mid-July that is associated with a filter change applied to the MD mode by the engineering team in an attempt to reduce the range sidelobes (which will be discussed further in Section 3). Before 7 July 2023, the mean daily mean offset is around 1.6 dB and after 7 July it is 1.3 dB.

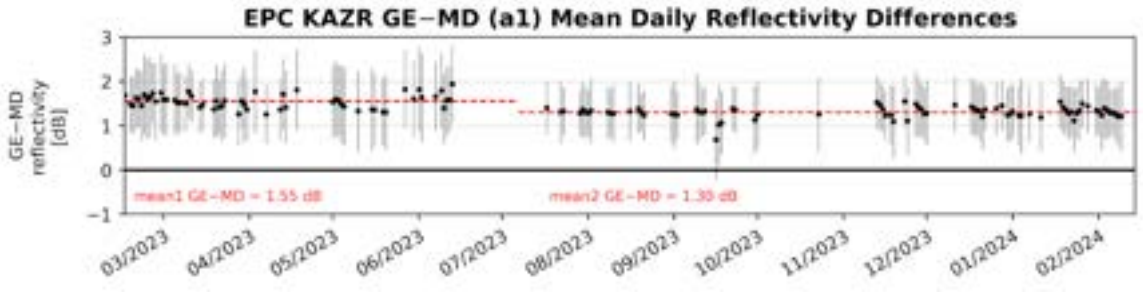

Figure 18. Time series of daily mean differences between KAZR a1 GE and MD mode reflectivity. The mean of the daily mean differences from 15 February to 7 July 2023 is 1.6 dB and the mean from 7 July 2023 to 14 February 2024 is 1.3 dB. The means are shown in the red dashed lines and the error bars represent standard deviation.

Since the GE mode offset was found to be about 3.4 dB, the two MD mode offsets applied for the first and second period were 5.0 dB and 4.7 dB (Table 3). The same comparison was run with the corrected KAZR data and the reflectivity between the two modes now agrees quite well (Figure 19).

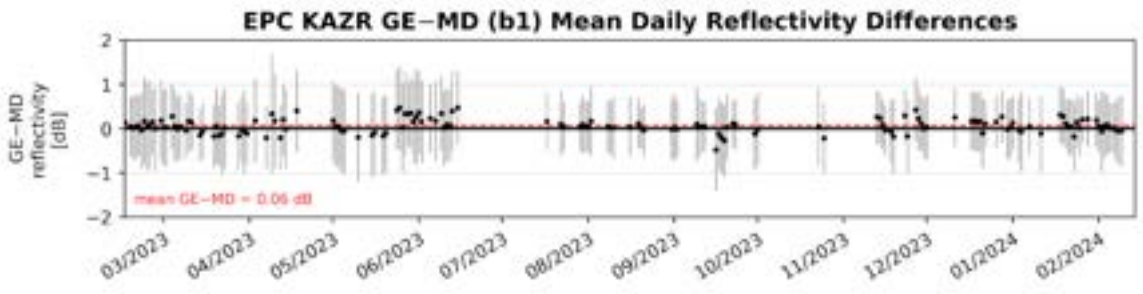

Figure 19. As in Figure 18 but after the GE and MD offsets have been applied. The mean of the daily mean differences between GE and MD modes is now 0.1 dB.

2.3 KaSACR Corrections

The corrected KAZR GE mode data can be used to calibrate the SACR reflectivity. This section describes the comparison specifically with KaSACR, which operates at a very similar frequency as KAZR. Given the paucity of vertically pointing scans by SACR and the fact that SACR and KAZR were not collocated (KAZR is about 3 km NNW of SACR), we apply a similar technique as KNKX versus KAZR from Section 2.2.1. The profiles over KAZR are extracted from the KaSACR PPIs, and the nearest KAZR gates in range and time are compared with the KaSACR profiles. Each PPI scan produces seven comparison points between KAZR and SACR. While RHI scans were performed by SACR over KAZR, the frequency of these scans was one every three hours. So, even though PPIs only produce a maximum of

seven comparison points per scan, PPIs occur every two minutes for most of the day, and thus comparisons with PPIs yield more data points.

Similar to KNKX versus KAZR, thresholds are applied to the data points to ensure attenuation is limited and that the radars are effectively seeing the same thing. For this analysis, both radars must have SNR greater than 0 dB and reflectivity between -5 and 15 dBZ. KAZR points also must have LDR less than -15 dB. Both KAZR and KaSACR reflectivity are corrected for gas attenuation, and only times when the relative humidity was less than 90% are considered. The daily mean differences and standard deviations between KaSACR and KAZR a1 reflectivity are then calculated and plotted in Figure 20. Only days when the number of points was greater than 10 and the standard deviation of the differences was less than 5 dB are shown. Overall, KAZR and KaSACR are in good agreement with one another. Prior to 12 March 2023, KaSACR is about 3.6 dB higher than KAZR. The difference decreases afterwards to around -0.8 dB. The KaSACR RF unit was replaced on 12 March, which explains this shift in reflectivity differences. Thus, the KaSACR reflectivity is corrected using two different values for the two time periods. After 12 March, KaSACR and KAZR agree well with reflectivity within 1 dB. There is some variability towards the end of the campaign, but no clear trend is visible. Additionally, a cluster of days with a large number of comparison points in early February 2024 shows the differences are right around 0 dB.

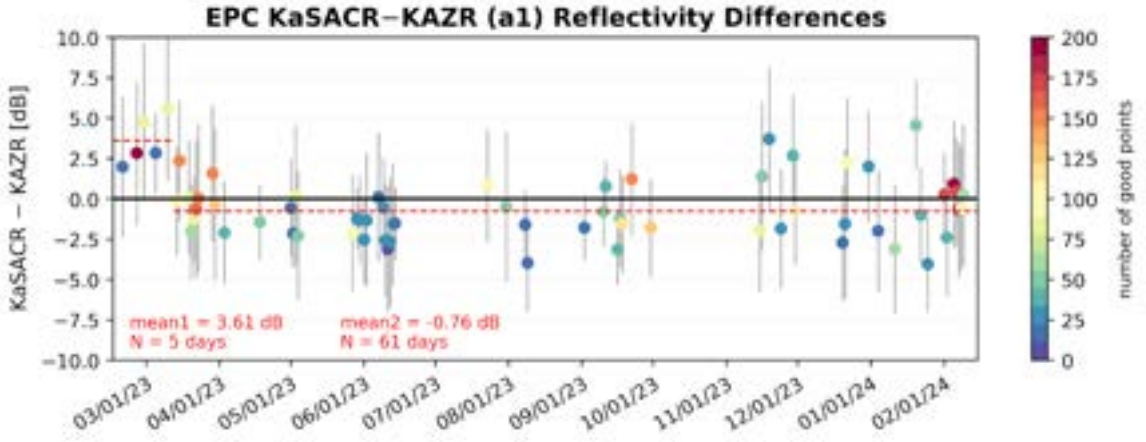

Figure 20. As in Figure 14 but for KaSACR and KAZR a1 reflectivity. Two lines are used to fit the data, one from 15 February to 12 March 2023 and the other from 12 March 2023 to the end of the campaign. The first offset is 3.6 dB while the second offset is -0.8 dB.

Since KAZR a1 reflectivity was found to be about 3.4 dB off (compared to KNKX and the disdrometer), the final offsets for KaSACR work out to be -0.2 dB from 15 February to 12 March 2023 and 4.2 dB for 12 March through 14 February 2024 (Table 3). The b1-level KAZR and KaSACR data agree well (Figure 21).

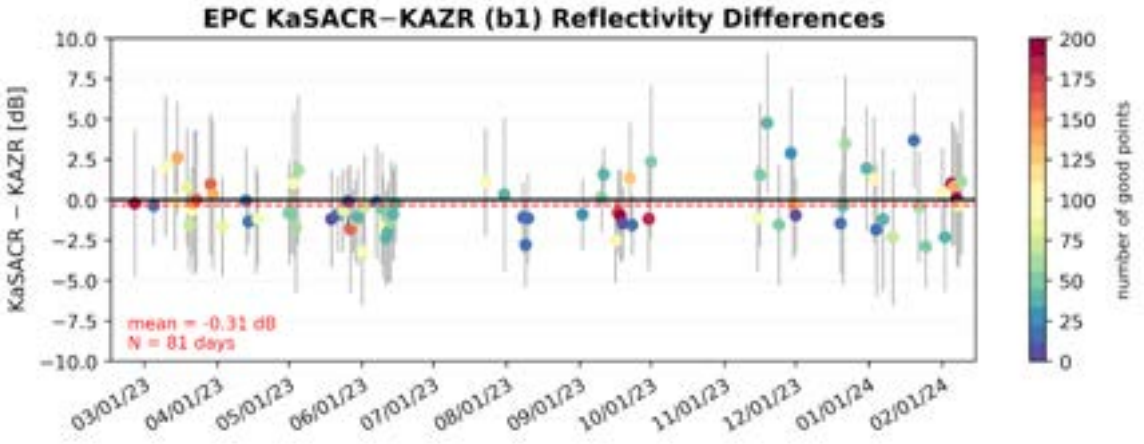

Figure 21. As in Figure 14 but with KAZR and KaSACR corrections applied. The mean reflectivity difference between KaSACR and KAZR is -0.3 dB.

2.4 WSACR Corrections

Similar to KaSACR, WSACR can also be calibrated based on the corrected KAZR GE mode data. Before the comparison is made, we first account for the declining transmit power (Figure 4). The radar constant is directly related to the transmit power, so a decrease in the transmit power will result in a decrease in reflectivity. We can use the original transmit power and the deviations from the original to calculate an initial bias. Figure 22 shows the offset needed to account for the transmitter decline, beginning on 12 March 2023. The slope is roughly 0.5 dB/month.

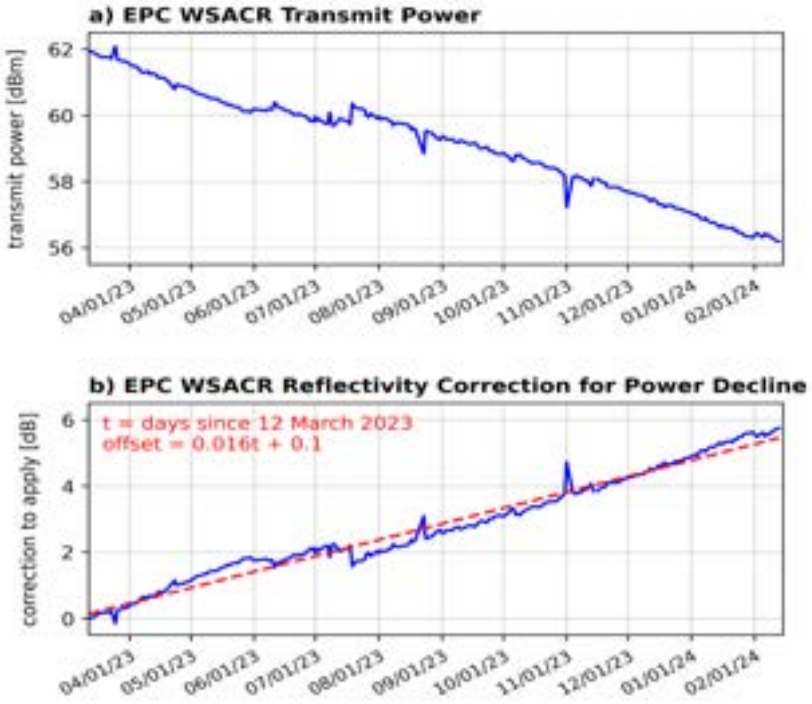

Figure 22. Time series of EPC WSACR (top) transmit power (dBm) and (bottom) reflectivity offset to apply to correct for the transmit power decline (dB).

After the WSACR is corrected for the transmit power, the same methodology that was used for the KaSACR comparison is also applied here for the WSACR comparison. A few differences are the thresholds applied to the comparison. The lower reflectivity threshold is extended to -15 dBZ to increase the number of valid points and an additional threshold for light rain is included (RR < 0.1 mm hr-1). This ensures only periods of clouds or very light rain are included in the analysis to eliminate further impacts from attenuation, particularly at W-band. Daily mean reflectivity differences between WSACR and KAZR are shown in Figure 23 and two periods are identified. The first period occurs prior to 12 March 2023 when the mean offset between WSACR and KAZR is 2.4 dB. The second period is after 12 March 2023, during which WSACR is about the same as KAZR on average. There is some variability across the time frame, but if we focus on a period in late May-early June when daily shallow clouds are present, we see the offset between WSACR and KAZR is near 0 dB (Figure 24).

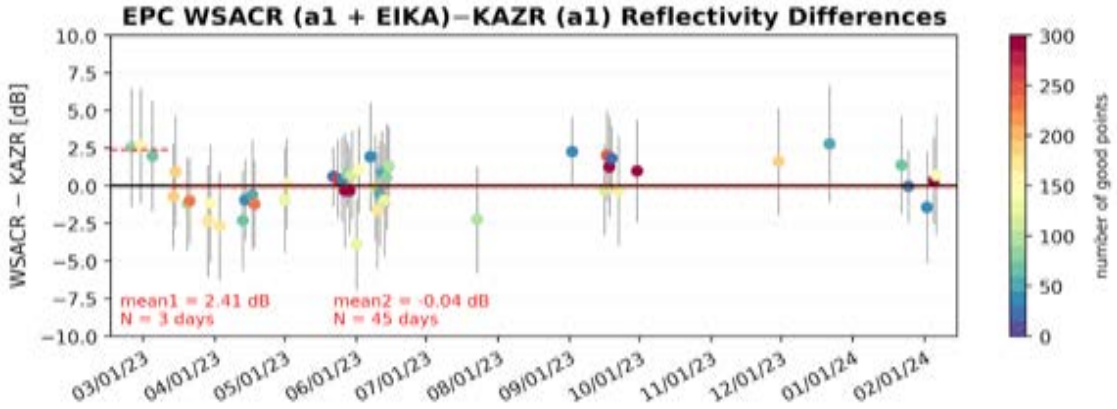

Figure 23. As in Figure 14 but for WSACR (after correction for power decline) and KAZR a1 reflectivity. Two lines are used to fit the data, one from 15 February to 12 March 2023 and the other from 12 March 2023 to the end of the campaign. The first offset is 2.4 dB and the second offset is 0.0 dB. These offsets are in addition to the offset calculated for the declining transmit power in Figure 22.

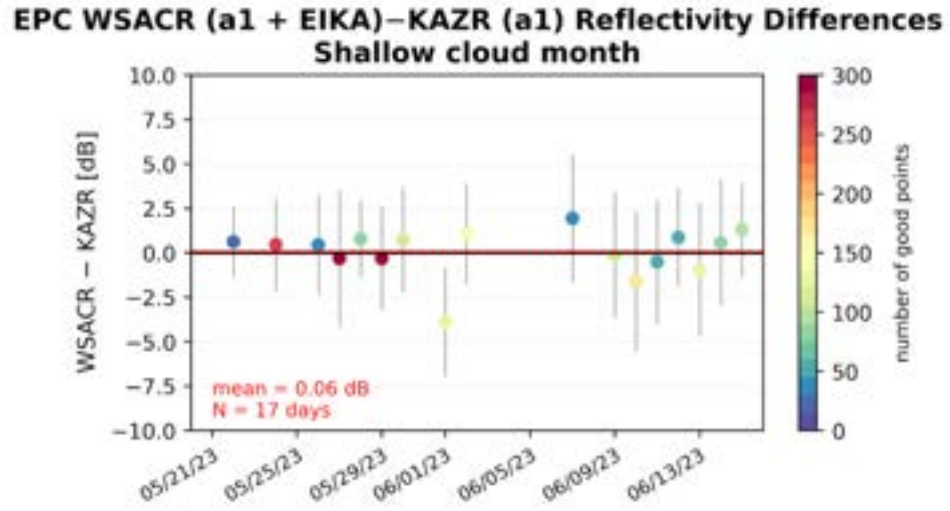

Figure 24. As in Figure 23 but zoomed in to 20 May-16 June 2023. The offset between WSACR and KAZR during this period of daily boundary-layer clouds is near 0 dB.

The final offset applied to WSACR reflectivity from 15 February to 12 March 2023 is 1.0 dB. The offsets starting 12 March are applied in a linear fashion following $0.016t + 3.5$ dB where t is the days since 12 March. The b1-level WSACR and KAZR data agree well after the offsets are applied (Figure 25).

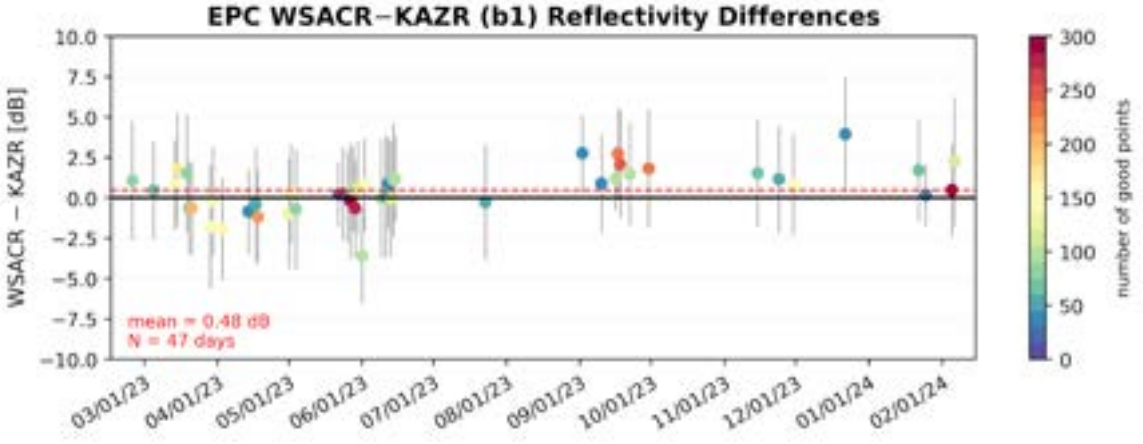

Figure 25. As in Figure 14 but with KAZR and WSACR corrections applied. The mean reflectivity difference between WSACR and KAZR is 0.5 dB.

3.0 Masks and Post-Processing

3.1 KAZR Masks

As in past ARM field campaigns, we develop a censor mask for KAZR using the velocity texture (spatial standard deviation of mean Doppler velocity). The velocity texture is calculated using the `calculate_velocity_texture` function in Py-ART and a 2.0 m s^{-1} threshold is used to distinguish between signal and background noise. An example of the censor mask applied to KAZR for the 18 September 2023 case is shown in Figure 26.

While velocity texture can be used to identify signals from background noise, it cannot alone distinguish between non-meteorological signals such as ground clutter, insects, and range sidelobes versus meteorological signals from clouds and precipitation. Thus, to help users further identify these signals, we develop a new non-meteorological echo classification mask for KAZR. The KAZR deployed during EPCAPE measured the signal LDR, which can be used to identify non-meteorological signals including insects. As will be discussed further in Section 3.3, insects were prevalent during EPCAPE and can be observed in the KAZR data on most days. In addition to insects/biota, stationary clutter is occasionally observed in the lowest few range gates of the KAZR GE mode. The clutter has near-zero Doppler velocity and spectral width. Range sidelobes in the KAZR MD mode are also visible when strong clouds or precipitation are present. This is a common feature of KAZR MD mode data, and previous work has been done to identify these features (Silber et al. 2018). Vertical gradients in SNR and spectral width are key to distinguishing between real cloud tops and sidelobe artifacts.

The resulting combination of methodologies to identify non-meteorological signals is shown in Figure 26 for the 18 September 2023 case. The four non-meteorological categories are background noise, ground clutter, sidelobe, and biota. Pixels that do not meet criteria for these categories are considered

hydrometeors. If users are only interested in meteorological data, they can use this mask to filter out the data of interest. The bottom panels of Figure 24 show reflectivity where only hydrometeors are present. Overall, the new mask performs quite well for this case, and the majority of the non-meteorological signals are identified and can be removed. One caveat of this mask is that it can misidentify weak cloud edges as biota, particularly in the MD mode.

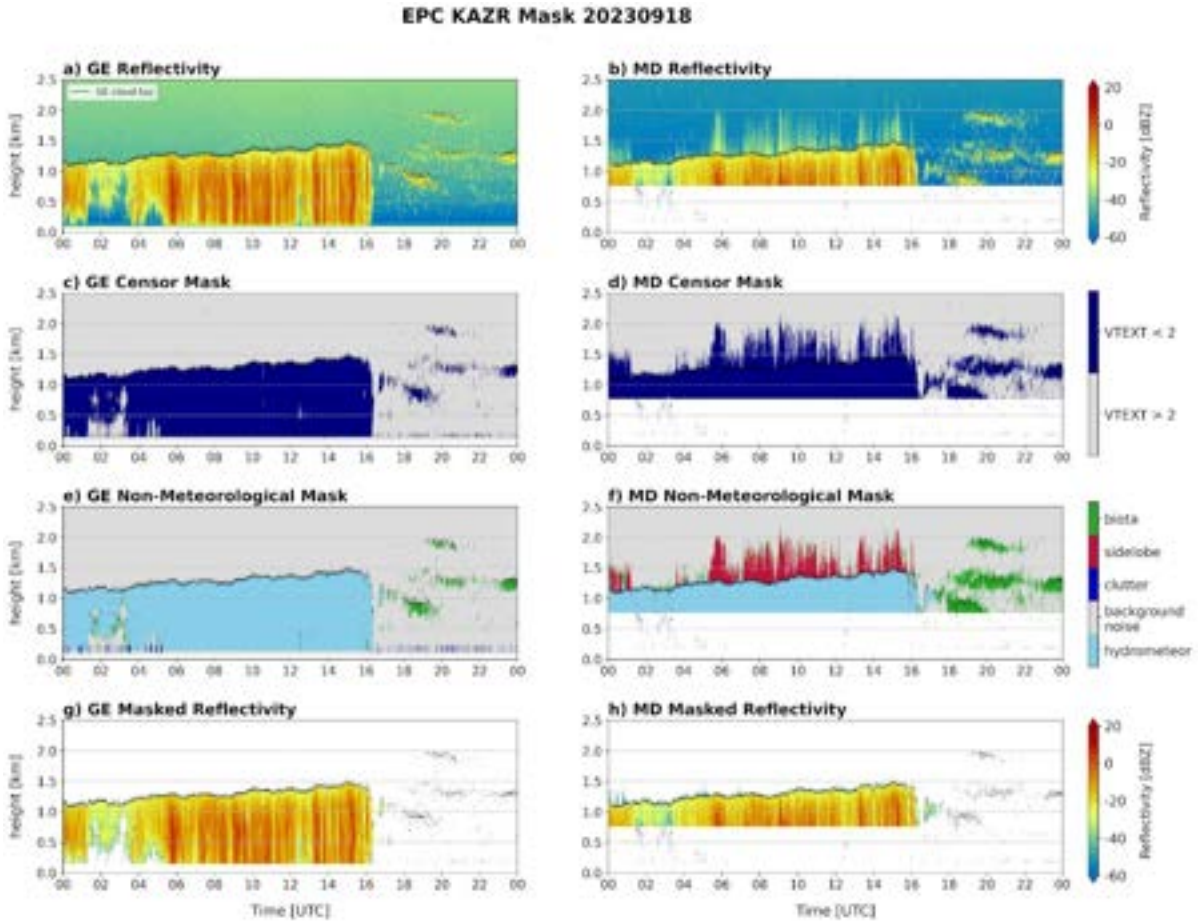

Figure 26. Time-height plots on 18 September 2018 of KAZR a-b) reflectivity (dBZ), c-d) censor mask (velocity texture > 2 m s^{-1} = light grey; < 2 m s^{-1} = navy blue), e-f) non-meteorological mask (hydrometeor = light blue; background noise = light grey; clutter = blue; sidelobe = red; biota = green), and g-h) reflectivity (dBZ) with non-meteorological signals masked out for GE mode (left) and MD mode (right). The GE mode cloud tops (based on an SNR threshold) are shown in black.

3.2 SACR Masks and Post-Processing

As with KAZR, SACR does not have any built-in masks for data-quality purposes. However, similar to KAZR, a simple censor mask was developed that distinguishes signals from background noise using the velocity texture (KaSACR) or SNR (WSACR). Different velocity texture thresholds were tested to see which preserved the most good data for KaSACR. Histograms of the velocity texture values calculated for both a PPI and RHI are shown in Figure 27. A shift in velocity texture values is observed in the KaSACR data set that corresponds to an increase in the Nyquist velocity (and also a decrease in the maximum

range). From the beginning of the campaign to when the change occurred on 18 May 2023, the velocity texture threshold used to distinguish signals from noise is 1.5 m s^{-1}. After 18 May, the best threshold is 2.0 m s^{-1}.

As shown in Figure 27, the use of velocity texture to distinguish between signal and background noise was also explored for WSACR. However, given the low Nyquist velocity (4.1 m s^{-1}), frequent velocity folding was observed in the data set, often resulting in higher velocity texture values that would have been considered background noise. Therefore, a simple SNR threshold was used for the WSACR censor mask instead. A threshold of -5 dB was found to mask the most background noise while still retaining hydrometeor information.

The resulting censor mask is shown for three SACR test files in Figure 28 along with other parameters including reflectivity, mean Doppler velocity, velocity texture, SNR, and the reflectivity with the censor mask applied. The censor mask generally performs quite well but can remove some signal, especially along velocity folds in KaSACR where the velocity texture is high.

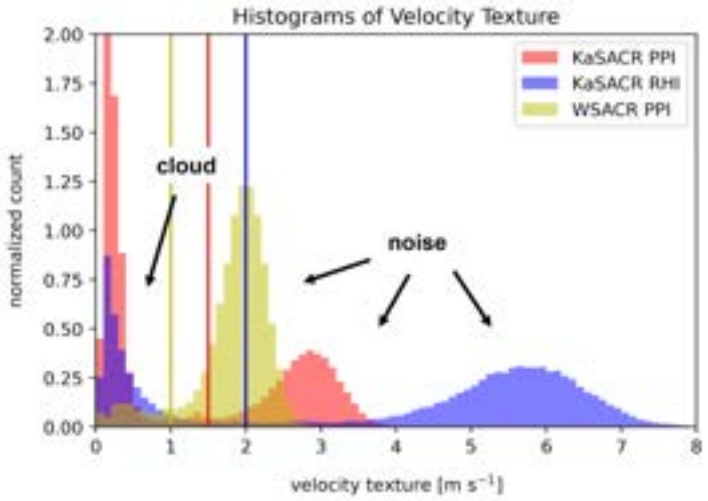

Figure 27. Histograms of velocity texture (m s-1) for three cases: KaSACR PPI on 29 March 2023 at 2030 UTC (red), KaSACR RHI on 21 January 2024 at 0111 UTC (blue), and WSACR PPI on 23 March 2023 at 1100 UTC (yellow). Peaks at higher velocity textures are related to background noise while peaks at lower velocity textures are due to signal returns. The thresholds chosen for the KaSACR censor mask are shown as the colored vertical lines and generally mark the boundary between signal and noise.

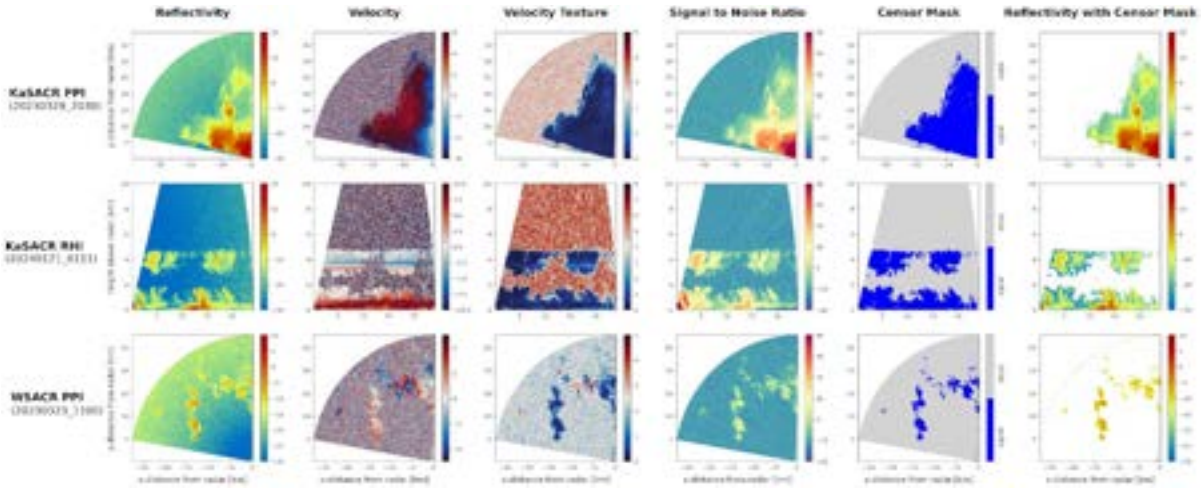

Figure 28. Panels of reflectivity (dBZ), mean Doppler velocity (m s-1), velocity texture (m s-1), SNR (dB), censor mask (signal versus background noise), and reflectivity with the censor mask applied (dBZ) for (top) KaSACR PPI on 29 March 2023 at 2030 UTC, (middle) KaSACR RHI on 21 January 2024 at 0111 UTC, and (bottom) WSACR PPI on 23 March 2023 at 1100 UTC.

In addition to a censor mask, a clutter mask for KaSACR was also developed. As mentioned in the RCA discussion (Section 2.1.2), the clutter signals observed by KaSACR during EPCAPE vary in time depending on the local environment. This makes it more challenging to identify clutter in the moments data, especially since the clutter reflectivity is often of similar magnitude as the meteorological echoes. Several sensitivity tests and combinations of parameters were tested to create the final clutter mask. The final clutter mask uses absolute mean Doppler velocity with textures of cross-polar differential phase (PhiDP-x), reflectivity, and spectral width. The textures are calculated over a 3x8 window (roughly 1 degree azimuth by 200 m range) using the `angular_texture_2d` function in Py-ART. After the censor mask is applied, several conditions need to be met in order for the pixel to be considered clutter:

1. Absolute mean Doppler velocity < 0.3 m s^{-1} AND
2. PhiDP-x texture > 50 degrees AND
3. Reflectivity texture > 3 dBZ AND
4. Spectral width texture > 0.15 m s^{-1}

If all these conditions are satisfied, the pixel is classified as potential clutter. The final clutter mask is then created by smoothing across the mask with a 5x5 window. Two examples of the clutter mask, one on a clear day and one on a cloudy day, are shown in Figure 29. While the clutter mask does a reasonable job at identifying ground targets, in some cases clutter can be misidentified as hydrometeors or vice versa. Misidentification has been most commonly observed in regions where the velocity is near 0 m s^{-1}. Therefore, users interested in specific cases may want to evaluate the performance of the mask on their own.

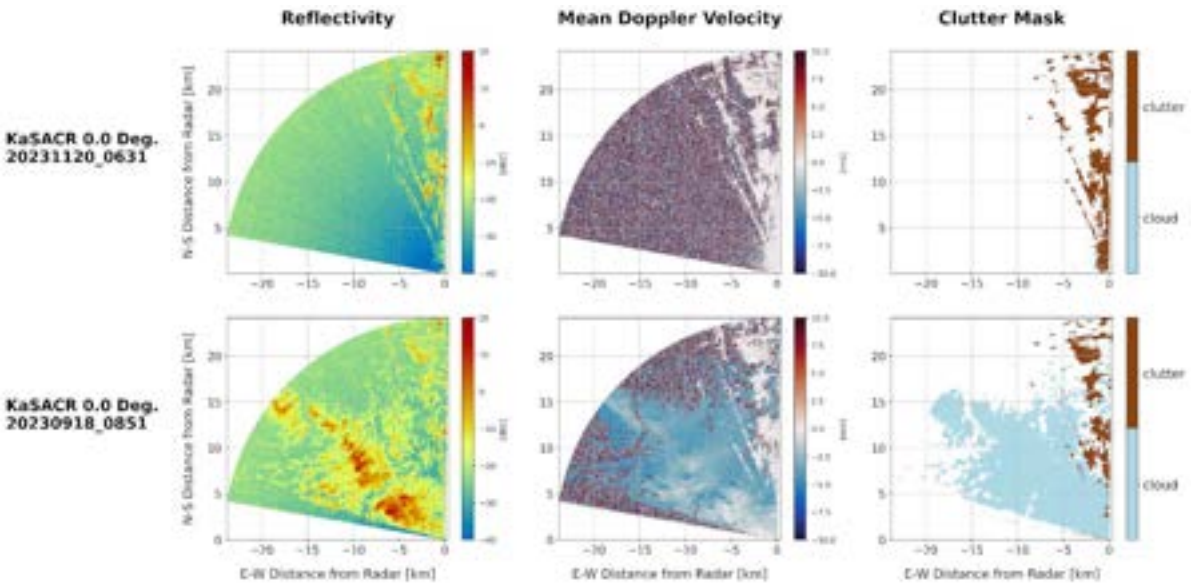

Figure 29. KaSACR PPIs at 0.0° of reflectivity (dBZ), mean Doppler velocity (m s^{-1}), and clutter mask for (top) 20 November 2023 at 0631 UTC and (bottom) 18 September 2023 at 0851 UTC.

3.3 Non-Meteorological Signals

Non-meteorological signals are frequently observed in the KAZR and SACR data throughout the campaign. These signals occur during the day (18-00 UTC; 11-17 LT), and are typically confined to the boundary layer, but can extend as far as 3.5 km above ground. After comparisons with several other instruments, these signals are thought to be from biota such as insects and/or birds. An example case of what these signals look like in the KAZR and KaSACR data is shown below.

Variables from the KAZR GE mode including reflectivity, Doppler velocity, LDR, and SNR are shown in Figure 30 for the 12 May 2023 case. The growth of shallow boundary-layer clouds below 1 km is observed starting at 02 UTC. Another feature is observed around 17 UTC at 2 km that has some similar characteristics to the boundary-layer clouds including similar reflectivity values (-20 dBZ), weak Doppler velocity (< 1 m s^{-1}), and SNR around 0 dB. However, the key difference is in the LDR field where this feature has LDR around -12 dB (compared to < -18 dB for clouds). Indeed, the KAZR insect mask that was developed and detailed in Section 3.1 indicates this feature is likely non-meteorological (Figure 30e).

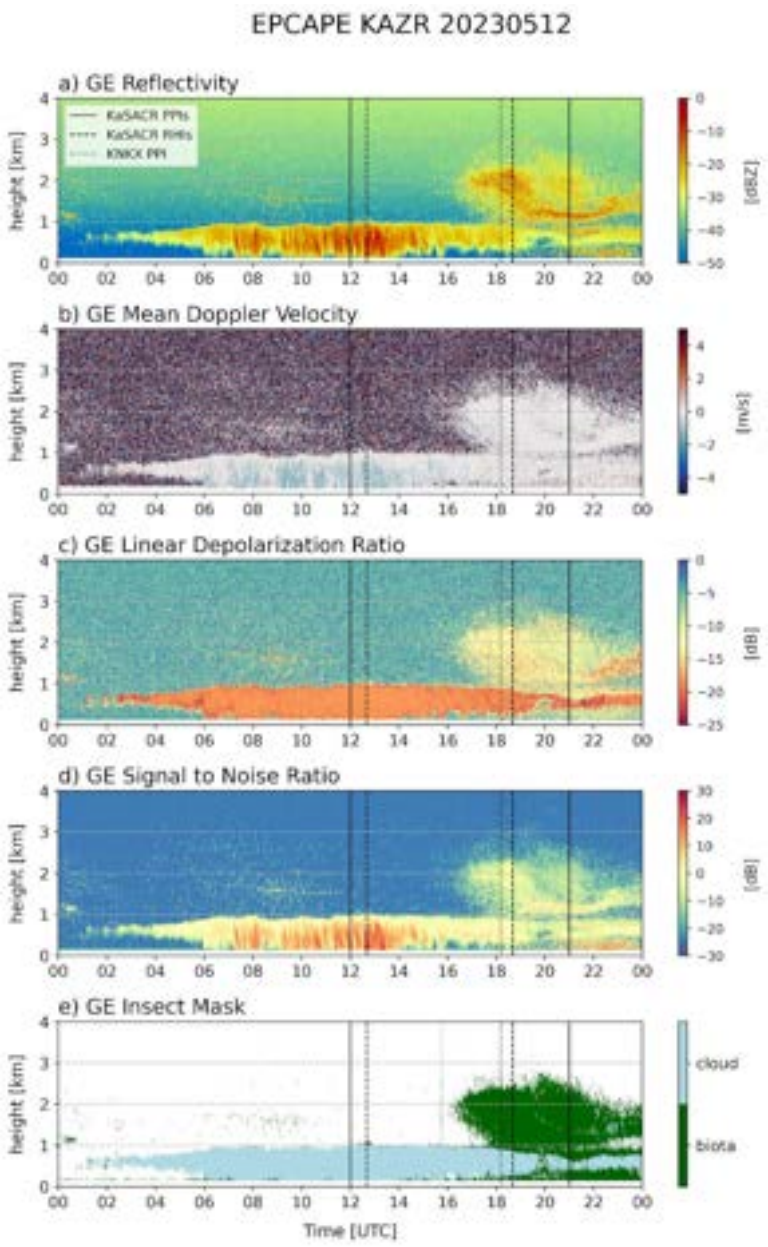

Figure 30. Time-height plots of KAZR GE mode a) reflectivity (dBZ), b) mean Doppler velocity (m s-1), c) LDR (dB), d) SNR (dB), and e) insect mask (green=biota; light blue=cloud) for the 12 May 2023 case. Solid (dashed) vertical lines correspond to KaSACR PPI (RHI) times shown in Figure 31 (32), and the dotted vertical line corresponds to the KNKX PPI time shown in Figure 33.

A PPI from KaSACR at 12 UTC shows small details in the cloud structure (Figure 31). Nine hours later at 21 UTC, the KaSACR PPI shows thin rings around the radar that correspond to shallow layers of non-meteorological signals. These layers have strong off-shore wind components. RHIs from KaSACR at times near the PPIs (1241 UTC and 1841 UTC) similarly show the differences between cloud and non-meteorological signals (Figure 32). The insects are observed at 1841 UTC around 1.5-2 km and are also associated with stronger off-shore flow.

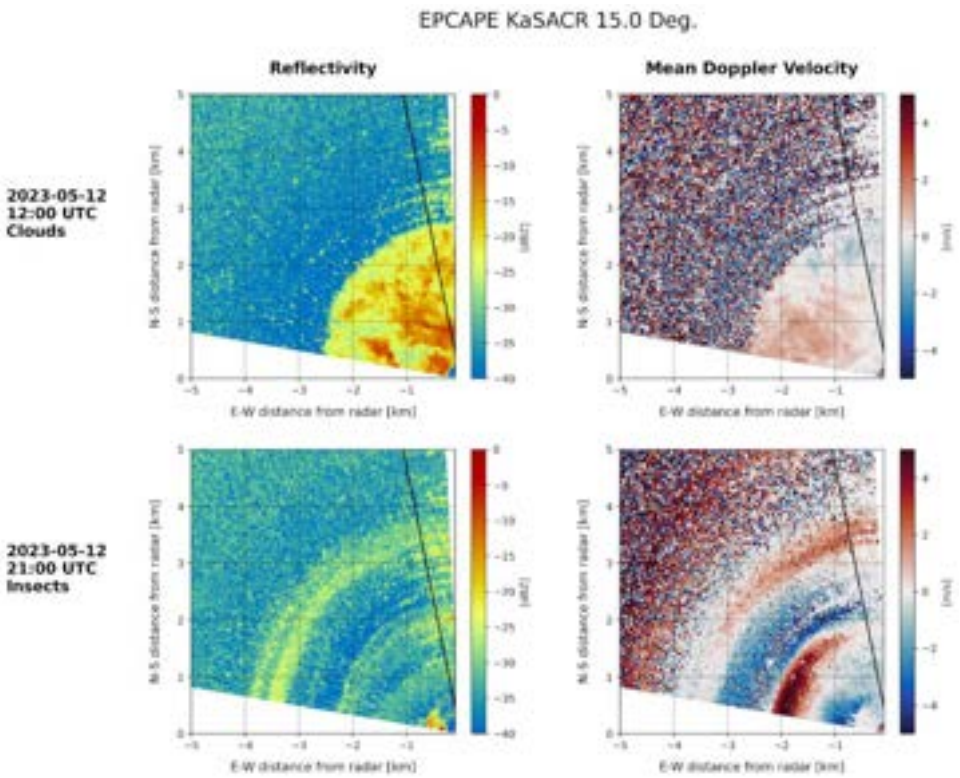

Figure 31. KaSACR PPIs at 15.0° of reflectivity (dBZ; left) and mean Doppler velocity (m s^{-1}; right) at 12 UTC (top) and 21 UTC (bottom) on 12 May 2023. PPIs are zoomed in to the nearest 5 km, and the solid line in each panel is the azimuth of KAZR (348.1°).

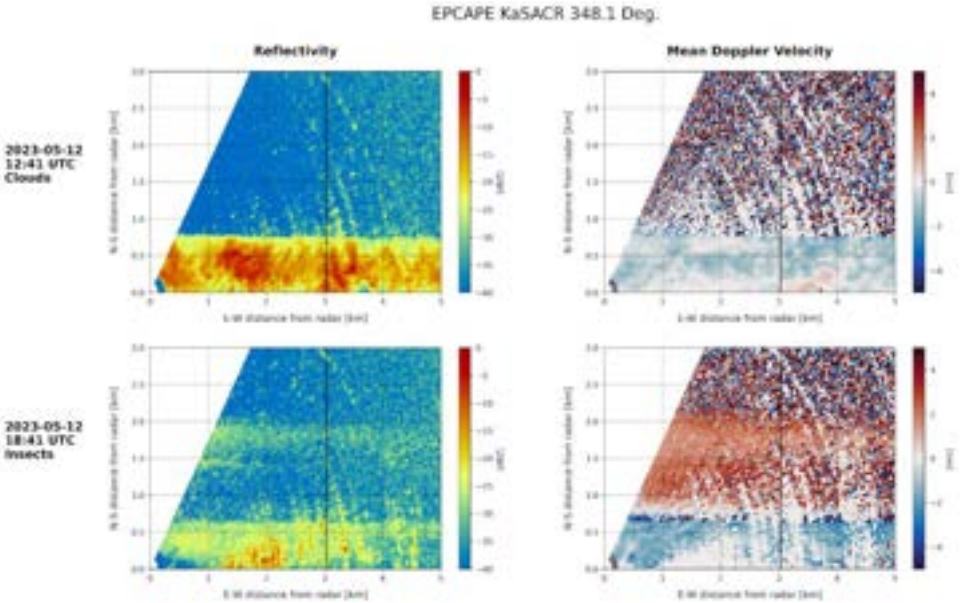

Figure 32. KaSACR RHIs at 348.1° of reflectivity (dBZ; left) and mean Doppler velocity (m s^{-1}; right) at 1241 UTC (top) and 1841 UTC (bottom) on 12 May 2023. RHIs are zoomed in to the nearest 5 km, and the solid line in each panel is the distance of KAZR (~3 km).

In addition to Ka-band data from the ARM radars, data from the local WSR-88D (KNKX) is analyzed to confirm that this feature is non-meteorological. KNKX is fully dual-polarization, which allows for the calculation of differential reflectivity (ZDR). ZDR is the ratio of the horizontal and vertical reflectivities, and non-meteorological signals such as insects often have very high ZDR values compared to clouds and precipitation. The KNKX PPI at 1811 UTC shows reflectivity values over the EPCAPE location around 0 dBZ, similarly strong off-shore flow, ZDR values greater than 8 dB, and low (< 0.95) RhoHV values (Figure 33). Radar echo classification from KNKX also indicates the signals observed are biota.

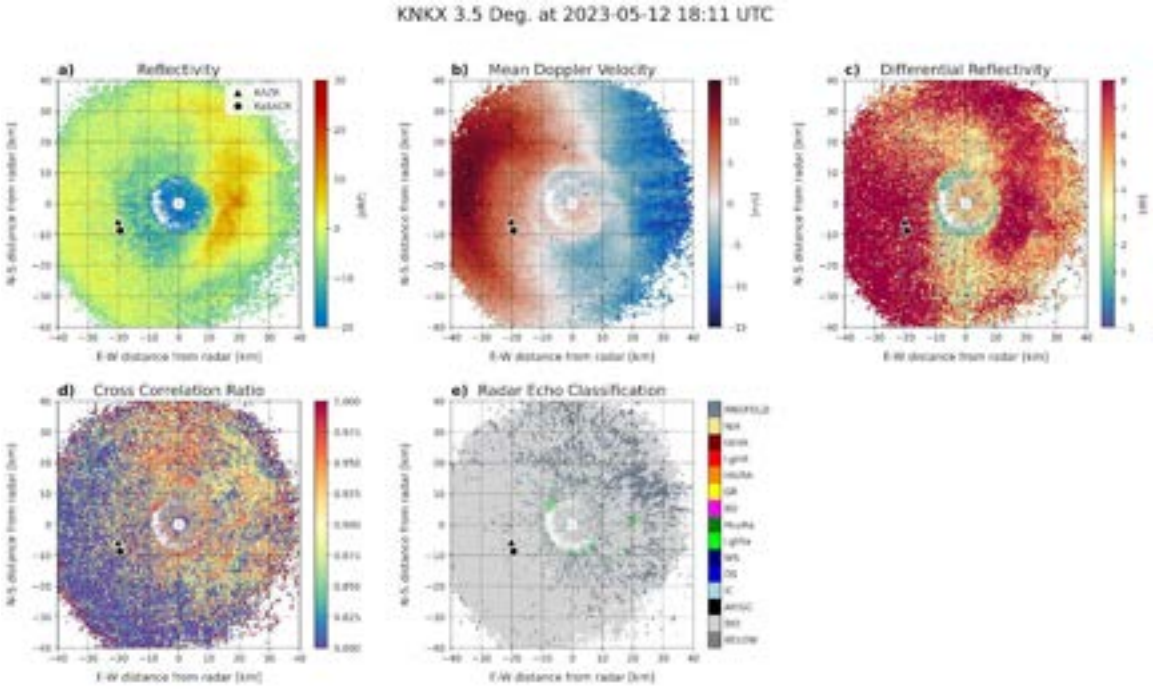

Figure 33. KNKX PPIs at 3.5° of a) reflectivity (dBZ), b) mean Doppler velocity (m s^{-1}), c) differential reflectivity (dB), d) cross-correlation ratio, and e) radar echo classification at 1811 UTC on 12 May 2023. PPIs are zoomed in to the nearest 40 km, and the triangle (circle) marker represents KAZR (SACR).

4.0 Description of Data Files

Some of the key variables in the b1-level radar datastreams for EPCAPE are listed below. The reflectivity fields have corrections applied to them (Table 3), and new masks detailed in Section 3 are included in the b1 data.

Key
New variable calculated in b1 data
Correction applied

KAZR File Contents (epckazrcfrgeqcM1.b1 and epckazrcfrmdqcM1.b1)	
Moments	
linear_depolarization_ratio	linear depolarization ratio, channel unspecified
mean_doppler_velocity	radial mean Doppler velocity, positive for motion away from the instrument
mean_doppler_velocity_crosspolar_v	Doppler velocity, cross-polar for vertical channel
reflectivity	equivalent reflectivity factor with offset applied
reflectivity_crosspolar_v	equivalent reflectivity factor, cross-polar for vertical channel
signal_to_noise_ratio_copolar_h	Signal-to-noise ratio, horizontal channel
signal_to_noise_ratio_crosspolar_v	Signal-to-noise ratio, cross-polar for vertical channel
spectral_width	spectral width
spectral_width_crosspolar_v	spectral width, cross-polar for vertical channel
Masks	
censor_mask	Bit mask 0: no mask 4: velocity_texture_above_threshold
classification_mask	Non-meteorological echo classification mask 0: hydrometeor 1: background noise 2: ground clutter 3: sidelobe 4: biota

KaSACR File Contents (epckasacrcfrqcS2.b1)	
Moments	
co_to_crosspol_correlation_coeff	Co-polar to cross-polar correlation coefficient (RhoXH)
crosspolar_differential_phase	cross-polar propagation phase shift
linear_depolarization_ratio_v	linear depolarization ratio, vertical channel
mean_doppler_velocity	radial mean Doppler velocity, positive for motion away from the instrument
reflectivity	equivalent reflectivity factor with offset applied
signal_to_noise_ratio_copolar_h	Signal-to-noise ratio, horizontal channel
signal_to_noise_ratio_crosspolar_v	Signal-to-noise ratio, cross-polar for vertical channel
spectral_width	spectral width
Masks	
censor_mask	Bit mask 0: no mask 4: velocity_texture_above_threshold
clutter_mask	Bit mask

KaSACR File Contents (epckasacrcfrqcS2.b1)	
	0: no mask 1: values within clutter thresholds

WSACR File Contents (epcwsacrcfrqcS2.b1)	
Moments	
co_to_crosspol_correlation_coeff	Co-polar to cross-polar correlation coefficient (RhoXH)
crosspolar_differential_phase	cross-polar propagation phase shift
linear_depolarization_ratio_v	linear depolarization ratio, vertical channel
mean_doppler_velocity	radial mean Doppler velocity, positive for motion away from the instrument
reflectivity	equivalent reflectivity factor with offset applied
signal_to_noise_ratio_copolar_h	Signal-to-noise ratio, horizontal channel
signal_to_noise_ratio_crosspolar_v	Signal-to-noise ratio, cross-polar for vertical channel
spectral_width	spectral width
Masks	
censor_mask	Bit mask 0: no mask 1: horizontal_snr_below_threshold

5.0 References

Deng, M, SE Giangrande, MP Jensen, K Johnson, CR Williams, JM Comstock, Y-C Feng, A Matthews, IA Lindenmaier, TG Wendler, M Rocque, A Zhou, Z Zhu, E Luke, and D Wang. 2025. "Wet-Radome Attenuation in ARM Cloud Radars and Its Utilization in Radar Calibration Using Disdrometer Measurements." *Atmospheric Measurement Techniques* 18(7): 1641–1657, https://doi.org/10.5194/amt-18-1641-2025

Feng, Y-C, A Matthews, M Rocque, M Deng, T Wendler, K Johnson, E Schuman, I Lindenmaier, V Castro, SE Giangrande, S Collis, R Jackson, A Theisen, and J Comstock. 2024. TRACER b1 Data Processing: Corrections, Calibrations, and Processing Report. U.S. Department of Energy, Atmospheric Radiation Measurement user facility, Richland, Washington. DOE/SC-ARM-TR-297.

Helmus, JJ, and SM Collis. 2016. "The Python ARM Radar Toolkit (Py-ART), a Library for Working with Weather Radar Data in the Python Programming Language." *Journal of Open Research Software* 4(1): e25., http://doi.org/10.5334/jors.119

Hunzinger, A, JC Hardin, N Bharadwaj, A Varble, and A Matthews, 2020. "An extended radar relative calibration adjustment (eRCA) technique for higher-frequency radars and range–height indicator (RHI) scans." *Atmospheric Measurement Techniques* 13(6): 3147–3166, https://doi.org/10.5194/amt-13-3147-2020

Matthews, A, K Johnson, E Schuman, Y-C Feng, S Matrosov, J Comstock, and SE Giangrande. 2023. MOSAiC Radar b1 Processing: Corrections, Calibrations, and Processing Report. U.S. Department of Energy, Atmospheric Radiation Measurement user facility, Richland, Washington. DOE/SC-ARM-TR-293.

Silber, I, J Verlinde, EW Eloranta, and M Cadeddu. 2018. "Antarctic cloud macrophysical, thermodynamic phase, and atmospheric inversion coupling properties at McMurdo Station: I. Principal data processing and climatology." *Journal of Geophysical Research – Atmospheres* 123(11): 6099–6121, https://doi.org/10.1029/2018JD028279

Silberstein DS, DB Wolff, DA Marks, D Atlas, and JL Pippitt. 2008. "Ground clutter as a monitor of radar stability at Kwajalein, RMI." *Journal of Atmospheric and Oceanic Technology* 25(11): 2037–2045, https://doi.org/10.1175/2008JTECHA1063.1

Ulaby, FT, RK Moore, and AK Fung. 1981. *Microwave Remote Sensing, Vol. I.* Addison-Wesley Publishing Company, Reading, Massachusetts.

Wolff, DB, DA Marks, and WA Petersen. 2015. "General Application of the Relative Calibration Adjustment (RCA) Technique for Monitoring and Correcting Radar Reflectivity Calibration." *Journal of Atmospheric and Oceanic Technology* 32(3): 496–506, https://doi.org/10.1175/JTECH-D-13-00185.1

Appendix A

KaSACR Sweeps and Negative Range

During EPCAPE, KaSACR experienced an issue in which the start and end indices of the sweeps were incorrect. This issue primarily occurred during the first third of the campaign from 15 February to 23 June. A fix for this sweep indexing issue was applied on the engineering side on 23 June, which mostly solved the issue except for a few random files. While the a1 data is still intact, typical plotting methods such as those used in Py-ART will not work.

The sweep indices are corrected in the b1-level data using the `determine_sweeps` function in Py-ART (version 1.17.0 or later), which uses the changes in elevation (for PPIs) or azimuth (for RHIs) to identify the start and end of the sweep. The `max_offset` parameter within the `determine_sweeps` function that best identifies the sweeps is 0.25 degrees (instead of the default 0.1 degrees). This is to account for the radar overshooting the elevation as the PPIs are performed. An example of the original and corrected start and end sweep indices with elevation and azimuth for a KaSACR file is shown in Figure 34. Note that in the original data there are five sweeps and the start and end of the sweeps occur when the radar is transitioning between elevation angles. In reality, the radar is only performing three sweeps, though, and the `determine_sweeps` function correctly identifies these three sweeps. Sweeps were identified using this method for all KaSACR b1 data. If users are interested in using a1-level data, they can also apply this method to correct the sweeps themselves.

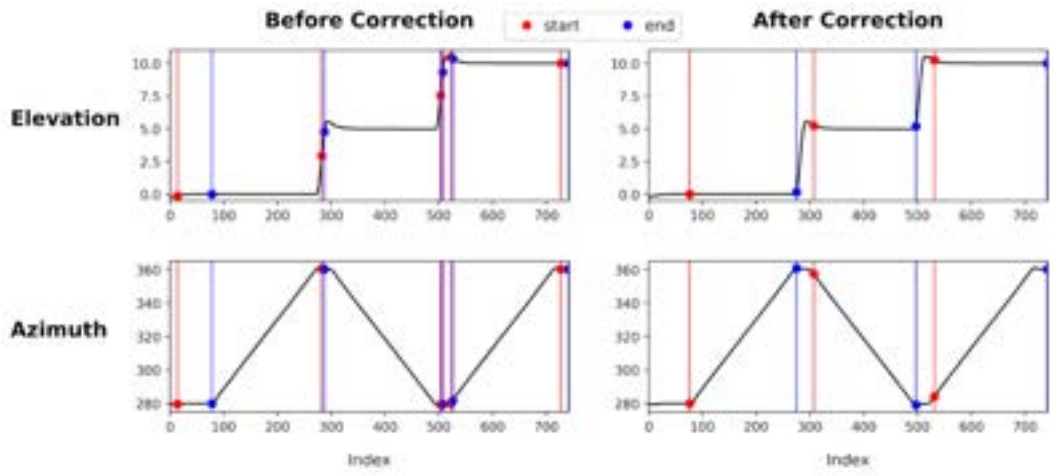

Figure 34. Elevation (top) and azimuth (bottom) profiles before the sweep correction (left) and after the sweep correction (right). Sweep start indices are shown in red and sweep end indices are shown in blue.

KaSACR also experienced another issue when it started recording data in the negative range. This issue started on 26 June and occurred until 15 November. The data in the negative range is internal noise from the radar and users interested in the data for meteorological purposes can ignore this. An example of data in the negative range is shown in Figure 35 in which the sky noise and cold noise, hot noise, main bang, and blind zone are all visible. While we do not remove this data in the b1-level files, plotting tools such as those in Py-ART will ignore data in the negative range. This data does not impact data in the normal radar range.

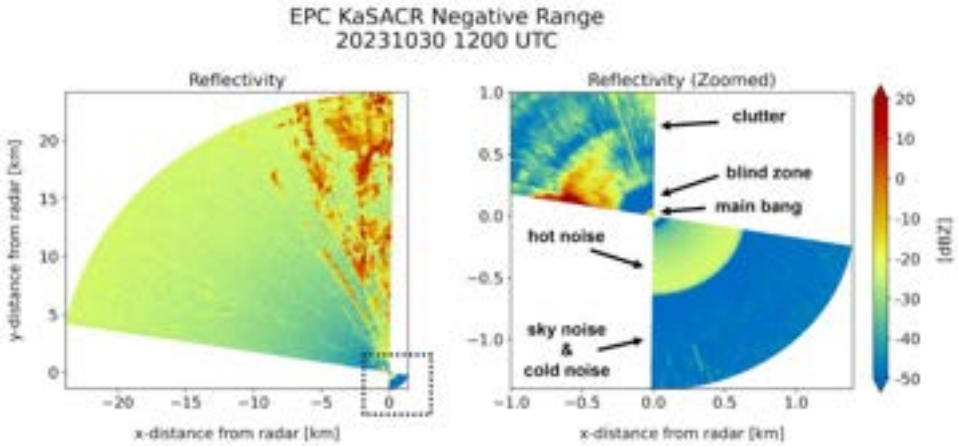

Figure 35. Reflectivity (dBZ) observed by KaSACR at 0.0° on 30 October 2023 at 12 UTC. The right panel is zoomed in to show data in the negative range, and different components of the internal noise measurements from the radar are annotated.

Appendix B

RCA Applied to KaSACR

RCA was also tested on a few clear days in August 2023 but with the 0.0° elevation PPIs (Figure 36). As mentioned in Section 2.1.2, the clutter at 0.0° is associated with anomalous beam propagation, which depends on the environmental conditions (particularly the vertical gradient in refractivity). Because of this, the ground clutter reflectivity appears to have a diurnal cycle, with larger reflectivity values observed in the afternoon hours. Thus, RCA cannot be used during EPCAPE to monitor the KaSACR stability. Additionally, few clutter signals are observed by the WSACR (not shown), which also limits RCA from being used to monitor the WSACR stability.

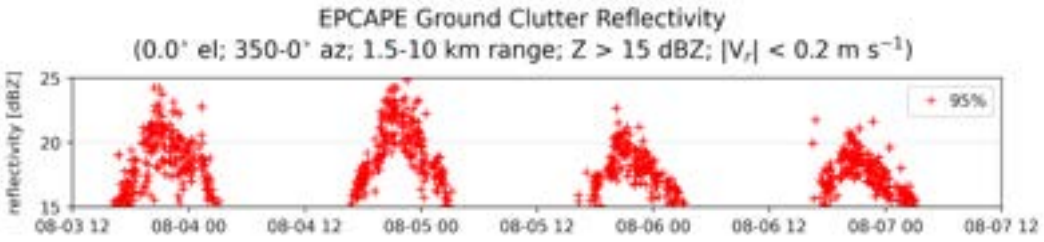

Figure 36. KaSACR RCA analysis from 3-7 August 2023 at 0.0° elevation.

Appendix C

Cross-Comparisons of KaSACR and KNKX

Another method using KNKX is applied to evaluate the calibration of KaSACR. Here, the `GateMapper` function in Py-ART is used to match gates from KaSACR and KNKX PPIs. Specifically for this analysis, the KaSACR data is mapped to the KNKX grid, which has coarser gate resolution. The default spatial (500 m) and temporal (60 s) thresholds are used to interpolate the nearest KaSACR gates to KNKX. An example of this mapping is shown in Figure 37, including the difference between KaSACR and KNKX.

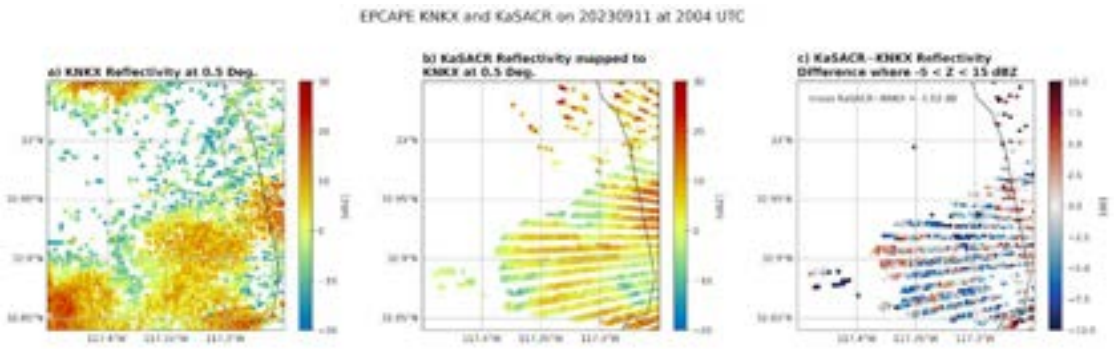

Figure 37. a) PPI of 0.5° reflectivity from KNKX, b) PPI of KaSACR reflectivity that has been mapped to 0.5° KNKX grid, and c) difference between KaSACR and KNKX reflectivity values that are between -5 and 15 dBZ. All PPIs are from 11 September 2023 at 2004 UTC. The mean reflectivity difference between KaSACR and KNKX at 0.5° for this time is -1.02 dB.

This method introduces more uncertainties compared to the KAZR versus KaSACR comparison detailed in Section 2.3. First, this analysis compares S-band data with Ka-band data. While reflectivity thresholds are applied to help reduce the uncertainties between the different frequencies, attenuation is still possible, which could contribute to the differences. Both gas and hydrometeor attenuation can be very high in the horizontal for Ka-band. This method also compares entire areas of data rather than single points, which can lead to increased variability.

The comparison between KaSACR and KNKX mapped areas is shown in Figure 38. The time series shows that KaSACR is around 5 dB lower than KNKX and each case has fairly high variability as noted by the large error bars. To show how the reflectivity varies on a case-by-case basis, Figure 39 shows histograms from a shallow cloud case on 11 June 2023 and a precipitation case on 21 January 2024. While there are noticeable differences in the distribution of points, the average difference when reflectivity values are between -5 and 15 dBZ is around 5 dB. Despite the larger variability, the final average is within 1 dB of the value determined from the KAZR versus KaSACR comparison (4.2 dB after March 12).

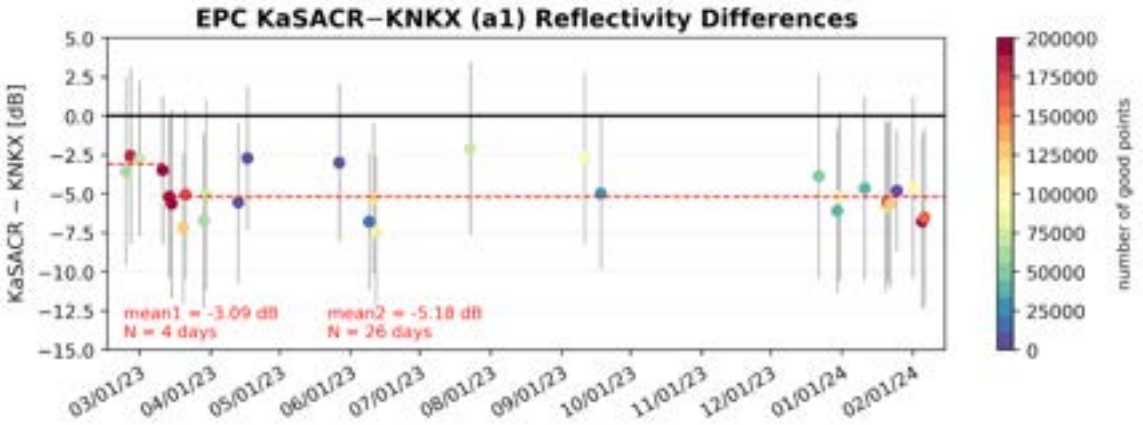

Figure 38. As in Figure 14 but for KaSACR and KNKX. Two lines are used to fit the data, one from 15 February to 12 March 2023 and the other from 12 March 2023 to the end of the campaign. The first offset is -3.1 dB while the second offset is -5.2 dB.

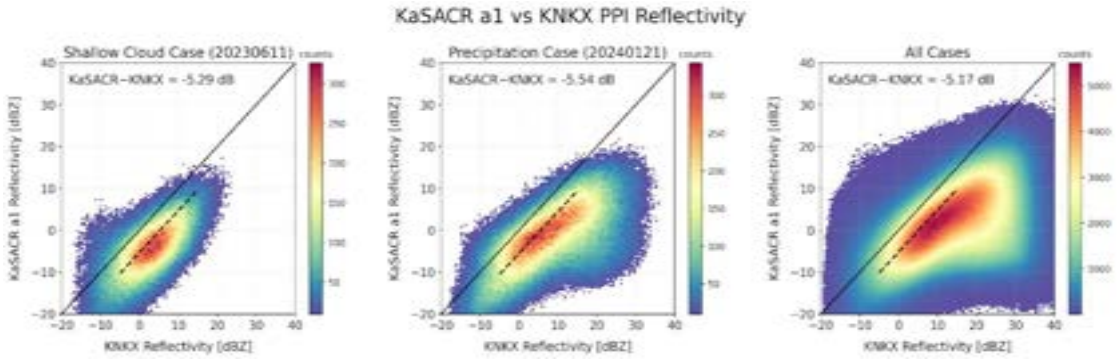

Figure 39. Histograms of KaSACR a1 reflectivity vs KNKX reflectivity for a) a shallow cloud case on 11 June 2023, b) a precipitation case on 21 January 2024, and c) for all cases. The one-to-one line is shown as the solid line and the line of best fit between -5 and 15 dBZ is shown in the dashed line. The average offset is shown in the upper left of each panel (around 5 dB).

www.arm.gov